Cell Host & Microbe

Potent SARS-CoV-2 neutralizing antibodies directed against spike N-terminal domain target a single supersite

Graphical abstract
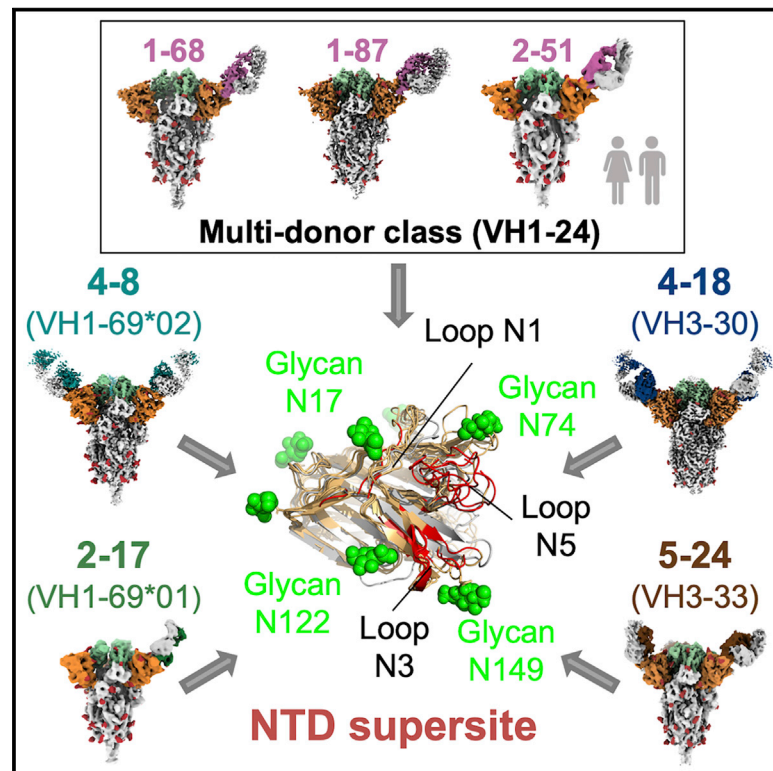
Authors

Gabriele Cerutti, Yicheng Guo, Tongqing Zhou, ..., Zizhang Sheng, Peter D. Kwong, Lawrence Shapiro

Correspondence

pdkwong@nih.gov (P.D.K.), lss8@columbia.edu (L.S.)

In brief

Cerutti et al. report structural analysis of seven potent neutralizing antibodies targeting the N-terminal domain of SARS-CoV-2 spike. All antibodies recognize a common glycan-free, electropositive surface comprised of a mobile β-hairpin and flexible loops. While RBD-directed antibodies recognize non-overlapping epitopes, these findings indicate that NTD-directed antibodies predominantly target a single supersite.

Highlights

- Structures of seven NTD-directed neutralizing antibody complexes with spike or NTD

- Structures define distinct recognition classes, one observed in multiple donors

- Supersite is glycan free, electropositive, with mobile β-hairpin and flexible loops

- Most potent NTD-directed neutralizing antibodies may target this supersite

CelPress

Article

Potent SARS-CoV-2 neutralizing antibodies directed against spike N-terminal domain target a single supersite

Gabriele Cerutti,[1,2,5] Yicheng Guo,[2,5] Tongqing Zhou,[3,5] Jason Gorman,[3] Myungjin Lee,[3] Micah Rapp,[1,2] Eswar R. Reddem,[1,2] Jian Yu,[4] Fabiana Bahna,[1,2] Jude Bimela,[1,2] Yaoxing Huang,[4] Phinikoula S. Katsamba,[1,2] Lihong Liu,[4] Manoj S. Nair,[4] Reda Rawi,[3] Adam S. Olia,[3] Pengfei Wang,[4] Baoshan Zhang,[3] Gwo-Yu Chuang,[3] David D. Ho,[4] Zizhang Sheng,[2,4] Peter D. Kwong,[1,3,*] and Lawrence Shapiro[1,2,3,4,6,*]

[1]Department of Biochemistry and Molecular Biophysics, Columbia University, New York, NY 10032, USA
[2]Zuckerman Mind Brain Behavior Institute, Columbia University, New York, NY 10027, USA
[3]Vaccine Research Center, National Institute of Allergy and Infectious Diseases, National Institutes of Health, Bethesda, MD 20892, USA
[4]Aaron Diamond AIDS Research Center, Columbia University Vagelos College of Physicians and Surgeons, New York, NY 10032, USA
[5]These authors contributed equally
[6]Lead contact
*Correspondence: pdkwong@nih.gov (P.D.K.), lss8@columbia.edu (L.S.)
https://doi.org/10.1016/j.chom.2021.03.005

SUMMARY

Numerous antibodies that neutralize SARS-CoV-2 have been identified, and these generally target either the receptor-binding domain (RBD) or the N-terminal domain (NTD) of the viral spike. While RBD-directed antibodies have been extensively studied, far less is known about NTD-directed antibodies. Here, we report cryo-EM and crystal structures for seven potent NTD-directed neutralizing antibodies in complex with spike or isolated NTD. These structures defined several antibody classes, with at least one observed in multiple convalescent donors. The structures revealed that all seven antibodies target a common surface, bordered by glycans $N17$, $N74$, $N122$, and $N149$. This site—formed primarily by a mobile β-hairpin and several flexible loops—was highly electropositive, located at the periphery of the spike, and the largest glycan-free surface of NTD facing away from the viral membrane. Thus, in contrast to neutralizing RBD-directed antibodies that recognize multiple non-overlapping epitopes, potent NTD-directed neutralizing antibodies appear to target a single supersite.

INTRODUCTION

Severe acute respiratory syndrome coronavirus 2 (SARS-CoV-2), the causative agent for coronavirus disease 2019 (COVID-19), emerged in 2019, rapidly establishing an ongoing worldwide pandemic with tens of millions infected and over one million dead (Callaway et al., 2020; Cucinotta and Vanelli, 2020; Dong et al., 2020). In response, an unprecedented global effort to develop vaccines and therapeutics is well underway. One promising approach is the identification of SARS-CoV-2-neutralizing antibodies, which could be used as therapeutic or prophylactic agents. Analysis of such antibodies can reveal viral sites of vulnerability to antibody neutralization, which can help guide the development of vaccines or therapeutics (Burton and Walker, 2020). The primary target for neutralizing antibodies is the viral spike protein, a trimeric type I viral fusion machine (Walls et al., 2020; Wrapp et al., 2020b) that binds virus to the ACE2 receptor on host cells (Benton et al., 2020; Yan et al., 2020; Zhou et al., 2020) and mediates fusion between the viral and cell membranes. The spike protein is comprised of two subunits: the S1 subunit comprising the N-terminal domain (NTD), the receptor-binding domain (RBD) and several other subdomains, and the

S2 subunit that mediates virus-cell membrane fusion (Walls et al., 2020; Wrapp et al., 2020b).

The majority of SARS-CoV-2 neutralizing antibodies so far identified target RBD (Brouwer et al., 2020; Cao et al., 2020; Chen et al., 2020; Chi et al., 2020; Ju et al., 2020; Liu et al., 2020b; Pinto et al., 2020; Robbiani et al., 2020; Rogers et al., 2020; Seydoux et al., 2020; Wang et al., 2020a; Wrapp et al., 2020a; Wu et al., 2020; Zeng et al., 2020; Zost et al., 2020). Structural studies (Barnes et al., 2020a, 2020b; Liu et al., 2020a; Wang et al., 2020b; Yuan et al., 2020b) and binding competition experiments (Liu et al., 2020a) have revealed neutralizing antibodies to recognize RBD at multiple distinct sites and further revealed multi-donor RBD-directed antibody classes that appear to be elicited with high frequency in the human population (Barnes et al., 2020b; Robbiani et al., 2020; Wu et al., 2020; Yuan et al., 2020b), as well as in mice with a humanized immune system (Hansen et al., 2020). Neutralization for many RBD-directed antibodies can be explained by interference with RBD-ACE2 interaction and/or impeding the ability of RBD to adopt the "up" conformation (Barnes et al., 2020b; Liu et al., 2020a; Yuan et al., 2020b) required for ACE2 binding (Benton et al., 2020).

NTD-directed neutralizing antibodies targeting the Middle East respiratory syndrome (MERS) betacoronavirus have been extensively characterized (Chen et al., 2017; Pallesen et al., 2017; Wang et al., 2018; Zhou et al., 2019). For SARS-CoV-2, three cryo-EM structures have been reported for NTD-directed neutralizing antibodies: 4A8 (Chi et al., 2020), FC05 (Wang et al., 2021), and CM25 (Voss et al., 2020) in complex with SARS-CoV-2 spike, the last two reported near the time of submission of this paper. NTD-directed antibodies have also been observed in electron microscopy (EM) analyses of antibodies from the sera of convalescent donors (Barnes et al., 2020b; Brouwer et al., 2020), and a low-resolution structure of a very potent antibody 4-8 has been reported (Liu et al., 2020a). This report was also notable for the identification of multiple NTD-neutralizing antibodies with potencies rivaling those of the best RBD-directed neutralizing antibodies.

Here, we describe cryo-EM and crystal structures for seven potently neutralizing antibodies in complex with either SARS-CoV-2 spike or NTD. We analyzed the genetic basis of recognition for each of the seven antibodies and further clustered them into antibody classes with similar genetics and modes of recognition. We also analyzed the antibody angles of approach and their recognized epitope. Remarkably, all seven antibodies targeted a single glycan-free surface of NTD, defining an NTD-antigenic supersite. We propose that all potently neutralizing NTD-directed SARS-CoV-2 neutralizing antibodies might target this site.

RESULTS

NTD-directed SARS-CoV-2 neutralizing antibodies
Prior studies have identified SARS-CoV-2-neutralizing antibodies that are S1-directed, but do not recognize RBD (Brouwer et al., 2020; Kreer et al., 2020; Rogers et al., 2020; Seydoux et al., 2020; Zost et al., 2020). Other studies have further delineated recognition and shown such antibodies to recognize NTD (Chi et al., 2020; Liu et al., 2020a; Zost et al., 2020). We identified a total of 17 published NTD antibodies, confirmed by the ELISA binding and competition data (Figure S1). We found that they derived from only nine VH genes, with antibodies originating from five genes (VH1-24, VH1-69, VH3-30, VH1-8, and VH4-39) evident in multiple donors. While these observations were sparse, they raised the possibility that NTD-directed neutralizing responses in different individuals could involve the convergent development of similar antibodies.

Structures for seven such antibodies in complex with SARS-CoV-2 spike or isolated NTD are presented below, grouped by VH gene.

NTD-directed neutralizing antibodies derived from VH1-24 represent a multi-donor class
Four NTD-directed neutralizing antibodies identified from convalescent donors—antibodies 1-68 and 1-87 from "donor 1," 2-51 from "donor 2" (Liu et al., 2020a), and antibody 4A8 from a third donor (Chi et al., 2020)—all of which derive from the *VH1-24* gene (Figure 1A). In addition to utilizing the same VH gene, three of these antibodies, 1-68, 1-87, and 4A8, utilized an identical set of heavy-chain-antibody genes—VH1-24, D6-19, and JH6—and showed significant similarity in their heavy chain third-comple-

mentarity-determining regions (CDR H3s), each of which was 21 amino acids in length (Figure S2). Antibody 2-51 also utilized VH1-24, but utilized different D and J genes, D6-13 and JH4, encoding a shorter CDR H3 region of only 14 amino acids. These VH1-24-derived antibodies utilized four different VL-genes: 1-87, 2-51, and 1-69 utilized lambda light chains VL2-14, VL2-8, and VL2-18, respectively, while 4A8 utilized kappa light chain VK2-24.

We determined cryo-EM structures for the spike complexes with antibodies 1-68, 1-87, and 2-51 at overall resolutions of 3.8, 3.63, and 3.71 Å, respectively (Figures 1B and S3A; Table S1). We also produced a locally refined cryo-EM map around the antibody:spike interface for 1-87 at 3.83-Å resolution, which allowed construction and refinement of an atomic model (Figure 1C). However, resolution in the antibody:spike interface region was blurred by domain motions for antibodies 2-51 and 1-68. We therefore produced crystals for 2-51 in complex with NTD, which provided an X-ray structure at 3.65-Å resolution (Figure 1D; Table S2).

Cryo-EM reconstructions of the VH1-24-derived 1-68, 1-87, and 2-51 antibodies each show a single Fab bound to the NTD of one subunit of the trimeric spike (Figure 1B). All antibodies target, with similar angle of approach, a single region on NTD—the loop region furthest from the spike-trimer axis. Moreover, the epitope and angle of approach for antibodies 1-68, 1-87 and 2-51 appear similar to those of antibody 4A8 (Chi et al., 2020), also derived from the VH1-24 gene.

Chi et al. (2020) defined the NTD loops in the 4A8-binding region as N1-N5 (corresponding to residue stretches 14 to 26, 67 to 79, 141 to 156, 177 to 186, and 246 to 260, respectively), and we adopt this nomenclature here. We note that the region defined as the N3 loop corresponds to a β-hairpin that includes both β strands that form a stem region and a short loop that connects them. The N1-N5 loops are disordered in most structures of spike, but some of these loops become ordered in antibody complexes. The structure of antibody 1-87 in complex with spike reveals almost all interactions to be mediated through heavy chain, with heavy chain accounting for 1057 Å^2 buried surface area and light chain 126 Å^2. The 19-residue CDR H3 loop provides the predominant interaction (Figure 1C, middle), with additional contributions mainly from CDR H1 (Figure 1C, right). CDR H3, which inserts between the N3 and N5 loops of NTD (Figure 1C, left) includes several hydrophobic residues (Ile96$_{HC}$, Val98$_{HC}$, Ile99$_{HC}$, Pro100b$_{HC}$, and Tyr100 h$_{HC}$) that interact with aromatic residues in N3, including Tyr145$_{NTD}$ and Trp152$_{NTD}$, and with hydrophobic residues of N5. Residues Ser100d$_{HC}$ and Asp101$_{HC}$ in CDR H3 also form hydrogen bonds with Trp152$_{NTD}$ and Gly252$_{NTD}$, respectively; the N-terminal glutamine residue of the heavy chain is also involved in hydrogen bonds with Ser254$_{NTD}$ and Ser255$_{NTD}$ in N5. Residues in CDR H1 form a network of hydrogen bonds involving positively charged residues from N3(Lys147$_{NTD}$), and N5(Arg246$_{NTD}$), with interactions by the side chains of CDR H1 residues Tyr27$_{HC}$ and Glu31$_{HC}$. Two additional VH1-24-gene-specific glutamic acid residues—Glu53$_{HC}$ in CDR H2 (Figure S4A)—and framework residue Glu71$_{HC}$ each participate in salt bridges with NTD. The only interaction mediated by the light chain is a hydrophobic interaction between Tyr49$_{LC}$ in CDR L2 and Pro251$_{NTD}$ in N5.
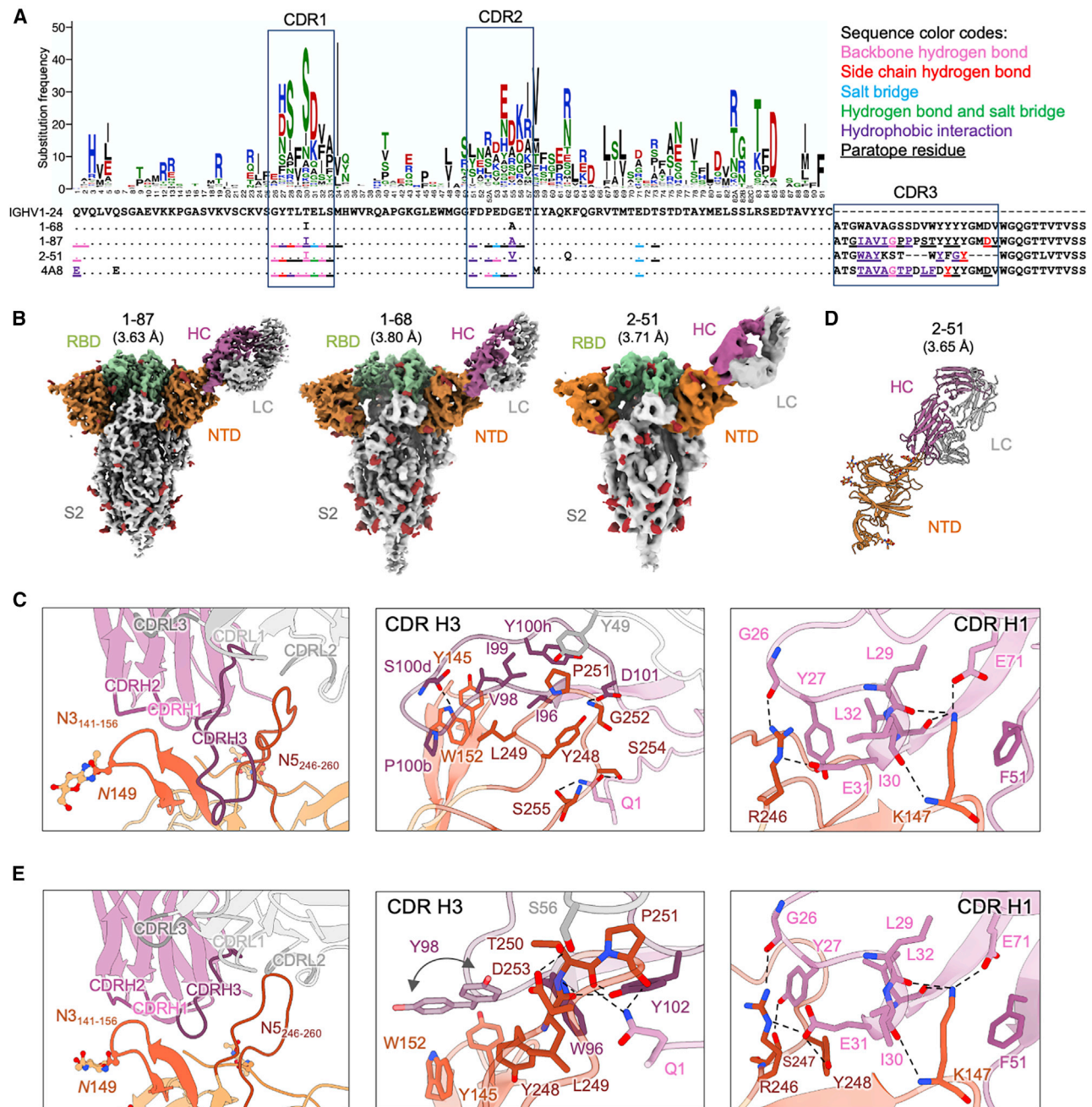
Figure 1. NTD-directed neutralizing antibodies derived from the VH1-24 gene define a multi-donor antibody class

(A) Sequence alignment of VH1-24-derived NTD-directed antibodies showing paratope residues, somatic hypermutations, and gene-specific substitution profile (GSSP) showing somatic hypermutation probabilities for VH1-24 gene. Antibody positions are assigned using the Kabat scheme, the CDRs are assigned by IMGT scheme. Paratope residues are highlighted by underscoring and colored by interaction types. Amino acids in GSSP are colored by chemical property.

(B) Cryo-EM reconstructions for spike complexes with antibodies 1-87, 1-68, and 2-51. NTD is shown in orange, RBD in green, and glycans in red, with antibody heavy chains in magenta and light chains in gray.

(C) Expanded view of 1-87 interactions with NTD showing overall interface (left), recognition by CDR H3 (middle), and recognition by CDR H1 (right). NTD regions N3 (residues 141–156) and N5 (residues 246–260) are colored in shades of orange; CDR H1, H2, and H3 are colored in shades of magenta; CDR L1, L2, and L3 are colored in shades of gray. Nitrogen atoms are colored in blue and oxygen atoms in red; hydrogen bonds (distance < 3.2 Å) are represented as dashed lines.

(D) Crystal structure of antibody 2-51 complexed with NTD, colored as in (B).

(E) Expanded view of 2-51 interactions with NTD showing overall interface (left), recognition by CDR H3 (middle), and recognition by CDR H1 (right), colored as in (C).

See also Figures S1–S7 and Tables S1 and S2.

The crystal structure of antibody 2-51 in complex with NTD reveals recognition remarkably similar to that of 1-87. The 14-residue CDR H3 loop of 2-51 inserts between the N3 and N5 loops of NTD (Figure 1E, left) with additional interactions from CDR H1. CDR H3 includes three aromatic residues (Trp96$_{HC}$, Tyr98$_{HC}$, and Tyr102$_{HC}$), which interact with aromatic residues in N3, including Tyr145$_{NTD}$ and Trp152$_{NTD}$, and with hydrophobic residues of N5, including Tyr248$_{NTD}$, Leu249$_{NTD}$, and Pro251$_{NTD}$ (Figure 1E, middle). The heavy chain Gln1$_{HC}$ residue is involved in hydrogen bonds with Thr250$_{NTD}$ and Pro251$_{NTD}$ in N5, similar to the hydrogen-bonding pattern observed for 1-87. The only interaction mediated by the light chain is a hydrogen bond between Ser56$_{LC}$ in CDR L2 and Asp253$_{NTD}$ in N5. Residues of CDR H1 form a network of hydrogen bonds nearly identical to the network formed in the 1-87 crystal structure (Figure 1E, right). Comparison of the 1-87 and 2-51 structures reveals a comparable level of similarity with VH1-24-derived antibody 4A8.

Overall, their common derivation from a common gene and highly similar recognition show the VH1-24 antibodies to define a multi-donor antibody class. Overall, the interaction is dominated by conserved contacts in CDR H1, along with hydrophobic interactions mediated by CDR H3. The VH1-24 gene restriction is explained partly by the conserved interactions of CDR H1, including those of the VH1-24-specific Glu31 and VH1-24-specific residues Glu53 and Glu71 (Figure S5A).

NTD-directed neutralizing antibodies derived from VH3-30 and VH3-33 genes show distinct recognition

Three neutralizing antibodies directed against NTD have been reported that derived from the highly similar VH genes VH3-30 and VH30-33. The high similarity of these genes, which encode only two amino acid differences between them (Figure 2A), raised the possibility that these antibodies might represent a multi-donor class despite their derivation from two distinct genes. We therefore determined cryo-EM structures for spike complexes with antibodies derived from each gene: antibody 4-18 from VH3-30 and antibody 5-24 from VH3-33 at 2.97 and 3.93 Å resolutions, respectively (Figures 2B–2C, S3B, and S3C; and Table S1).

The cryo-EM structure of antibody 4-18 in complex with spike reveals an epitope that overlaps the VH1-24 antibodies, but with a significantly different overall mode of recognition. Overall, interactions are primarily mediated by CDR H2 and CDR L3, with additional contributions from CDRs H3, L1, and L2 (Figure 2D, left; Figure S4B). While CDR H3 inserts between NTD loops N3 and N5 like VH1-24 antibodies, the light chain CDR L3 binds adjacent to this region and also forms interactions with the NTD N1 loop. CDR H2 mediates extensive hydrogen bonding and hydrophobic interactions with NTD (Figure 2D, middle). CDR H2 residues Ser55$_{HC}$ and Asn56$_{HC}$ form hydrogen bonds with both backbone and side chain of Asn17$_{NTD}$ at the base of the NTD N17 glycan in the N1 region. CDR H2 residues Ser52$_{HC}$ and His58$_{HC}$ also form hydrogen bonds with Tyr248$_{NTD}$ in N5. Hydrophobic interactions are observed for CDR H2 residue Val50$_{HC}$ with Leu249$_{NTD}$ and Tyr52a$_{HC}$ with Pro251$_{NTD}$ in N5. In the light chain, Tyr95b$_{LC}$ from the CDR L3 loop hydrogen bonds with glycan N17 (Figure 2D, right) within the N-terminal region, which is typically disordered in ligand-free spikes.

Despite containing multiple aromatic residues in CDR H3, for the most part, these residues do not form substantial hydrophobic interactions with residues from NTD, with exceptions of Tyr98$_{HC}$ and Tyr100$_{HC}$, which bury 98 and 205 Å^2 accessible surface area in the interface, respectively (Figure S4B, left). Rather, the primary interactions mediated by CDR H3 are hydrogen bonds, including from the backbone carbonyl of Tyr98$_{HC}$ with the backbone amide of NTD Ser247$_{NTD}$ and a hydrogen bond from the side chain hydroxyl of Tyr100$_{HC}$ with the side chains from NTD residues Glu156$_{NTD}$ and Arg158$_{NTD}$.

The structure of VH3-33-derived antibody 5-24 (Figure 2C) in complex with spike reveals targeting of an overlapping epitope in NTD, but with overall recognition mediated by CDR H3 with additional contributions from CDR H1, but without the involvement of CDR L3 as seen for antibody 4-18 (Figure 2E, left). Also different from 4-18, four aromatic residues in the CDR H3 region of antibody 5-24 make extensive hydrophobic contacts with NTD loop N5 and the stem of the N3 β-hairpin (Figure 2E, middle), distinct from the hydrogen bond-dominated recognition observed in 4-18; recognition by other CDRs is also different.

Overall, while they target overlapping regions in NTD, recognition by VH3-33-derived antibody 5-24 is substantially different from that mediated by VH3-30-derived antibody 4-18. These dissimilarities show that, despite their derivation from highly similar VH genes, the NTD-directed neutralizing antibodies from VH3-30 and VH3-33 are not members of a single antibody class. Structural analysis showed that Ser52$_{HC}$ from VH3-30 forms a hydrogen bond with Tyr248$_{NTD}$. Substitution of Ser52$_{HC}$ with the VH3-33-encoded Trp would lead to significant clashes with residues in CDR H2 and NTD loops N1 and N5 (Figure S4C), which could abolish the interaction between 4-18 and NTD. This suggests that the VH3-33 antibodies containing Trp52$_{HC}$ cannot recognize NTD through a binding mode similar to VH3-30 antibody 4-18.

NTD-directed neutralizing antibodies derived from the VH1-69 gene appear to comprise both reproducible and distinct classes

Of the 17 currently characterized NTD-directed or likely NTD-directed neutralizing antibodies (Figure S1A), three—antibodies 2-17 and 4-8 (Liu et al., 2020a) and antibody COV2-2676 (Zost et al., 2020)—derived from the VH1-69 gene, with antibodies 2-17 and 4-8 deriving from the VH1-69*01 and VH1-69*02 alleles, respectively (Figure 3A). Further, the CDR L3 regions of 2-17 and COV2-2676 showed high similarity (Figure 3E). To understand the recognition of these VH1-69-derived antibodies, we determined cryo-EM structures for spike complexes with the two most potent: antibodies 2-17 and 4-8 with IC$_{50}$ potencies of 0.007 and 0.009 μg/mL.

Single-particle cryo-EM data for antibody 4-8 yielded a 3D reconstruction at 3.25-Å resolution (Figures 3B and S3D; Table S1); however, like antibody 2-17 (Figures 3C and S3E; Table S1), and as reported previously (Liu et al., 2020a), high mobility of the bound Fab blurred the interface region. We used local refinement with particle subtraction to obtain a high-quality reconstruction for the 4-8 interface with spike (Figure 3D). Like the VH1-24-derived antibodies, CDR H3 binds between the NTD N3 and N5 loops, but in a distinctive way; CDR H3 dominates the interface and its approach to the N3/N5 region is nearly
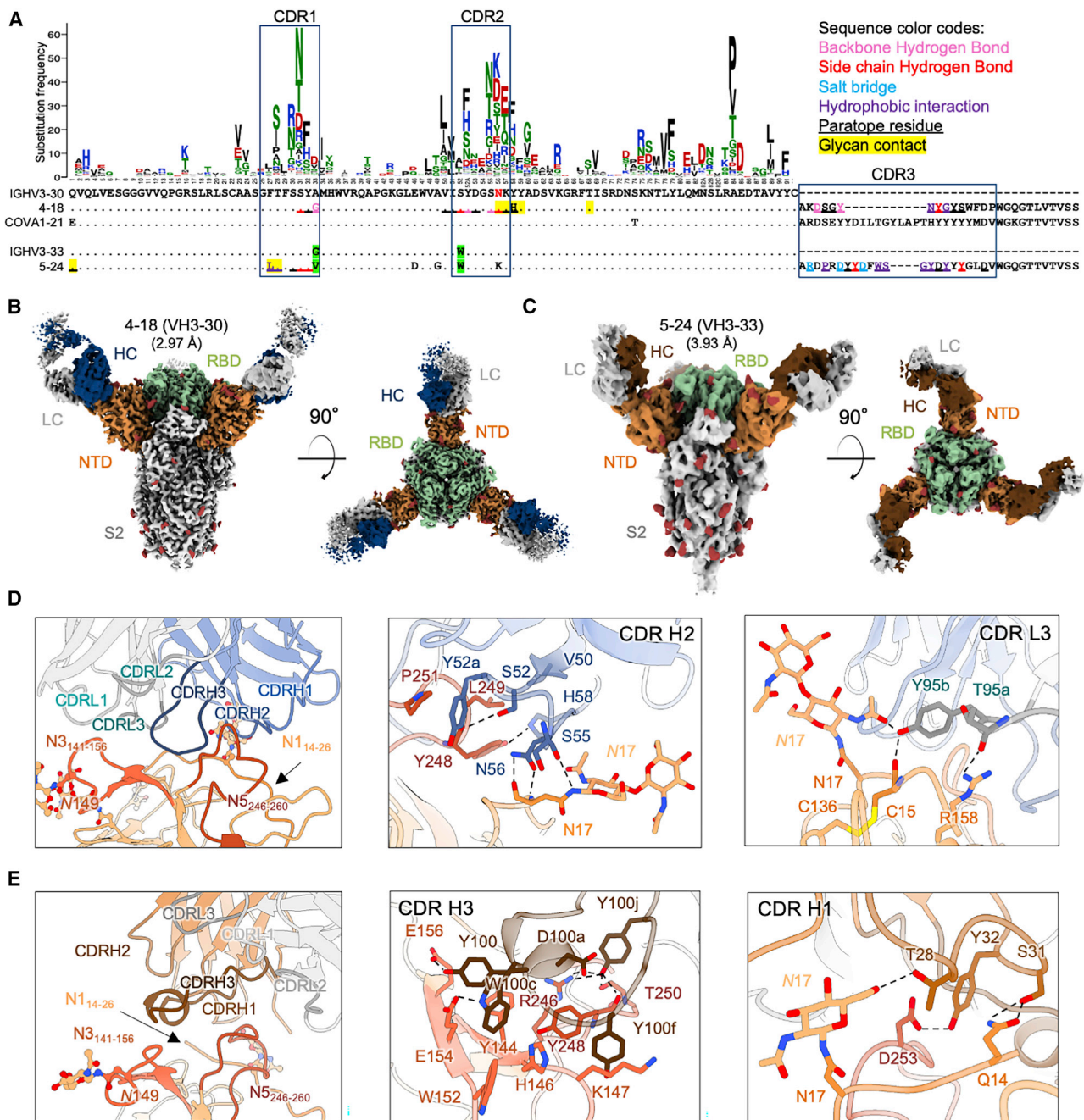
Figure 2. NTD-directed neutralizing antibodies derived from the closely related VH3-30 and VH3-33 genes show distinct binding modes

(A) Sequence alignment of VH3-30-derived (4-18) and VH3-33-derived (5-24) NTD-directed antibodies showing paratope residues, somatic hypermutations, and gene-specific substitution profile (GSSP) showing positional somatic hypermutation probabilities for VH3-30 gene. Substitutions between VH3-30 and VH3-33 germline genes are highlighted in green.

(B) Cryo-EM reconstruction for spike complex with antibody 4-18 from two orthogonal views; NTD is shown in orange, RBD in green, and glycans in red, with antibody heavy chain in blue and light chain in gray.

(C) Cryo-EM reconstruction for spike complex with antibody 5-24 from two orthogonal views; NTD is shown in orange, RBD in green, and glycans in red, with antibody heavy chain in brown and light chain in gray.

(D) Expanded view of 4-18 interactions with NTD showing the overall interface (left), recognition in CDR H2 (middle), and recognition in CDR L3 (right). NTD regions N1 (residues 14–26), N3 (residues 141–156), and N5 (residues 246–260) are shown in shades of orange; CDR H1, H2, and H3 are shown in shades of blue; CDR L1, L2, and L3 are shown in shades of gray.

(E) Expanded view of 5-24 interactions with NTD showing the overall interface (left), recognition in CDR H3 (middle), and recognition in CDR H1 (right), colored as in (D) except for CDR H1, H2, and H3, which are colored in shades of brown.

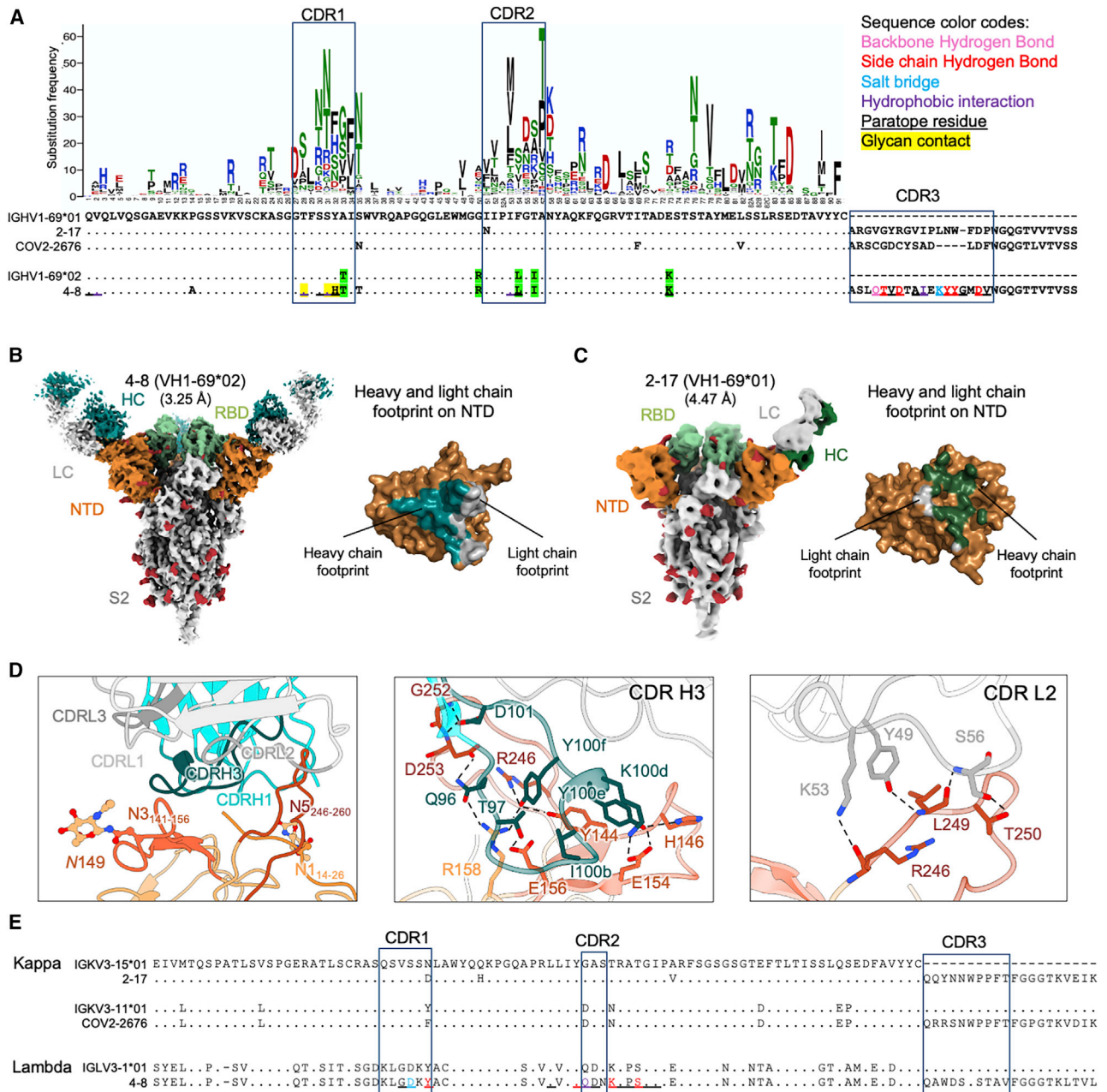See also Figures S1, S3, and S6, and Table S1.

Figure 3. NTD-directed neutralizing antibodies derived from the closely related VH1-69*01 and VH1-69*02 genes show distinct binding modes

(A) Sequence alignment for VH1-69*01-derived (2-17) and VH1-69*02-derived (4-8) NTD-directed antibodies showing somatic hypermutations and paratope residues, with gene-specific substitution profile (GSSP) showing positional somatic hypermutation probabilities for VH1-69. Residues that differ between VH1-69*01 and VH1-69*02 alleles are highlighted in green.

(B) Cryo-EM reconstruction for spike complex with antibody 4-8; NTD is shown in orange, RBD in green, glycans and in red, with antibody heavy chain in teal and light chain in gray. Heavy and light chain footprint on NTD (right).

(C) Cryo-EM reconstruction for spike complex with antibody 2-17 (left); NTD is shown in orange, RBD in green, and glycans in red, with antibody heavy chain in dark green and light chain in gray. Heavy and light chain footprint on NTD (right, NTD shown with template-based modeling).

(D) Expanded view of 4-8 interactions with NTD showing the overall interface (left), recognition in CDR H3 (middle), and recognition in CDR L2 (right). NTD regions N1 (residues 14–26), N3 (residues 141–156), and N5 (residues 246–260) are shown in shades of orange; CDR H1, H2, and H3 are shown in shades of teal; CDR L1, L2, and L3 are shown in shades of gray.

(E) Sequence alignment of light chain of VH1-69-derived antibodies showing diverse germline gene usage (2-17 and COV2-2676 utilizes kappa light chain; 4-8 utilizes lambda light chain); IGKV3-15*01 is used as reference. Paratope residues of 4-8 are colored as in (A).

See also Figures S1, S3, and S6, and Table S1.

orthogonal to that observed for CDR H3 in the VH1-24 class antibodies (Figure 3D, middle). Recognition by other CDRs is also distinct from the other NTD-directed neutralizing antibodies (Figure 3D, right; Figure S4D)

We also collected single-particle cryo-EM data for antibody 2-17, yielding a 3D reconstruction at 4.47-Å resolution (Figures 3C and S3E; Table S1). Despite the poor resolution of the 2-17 cryo-EM maps, we were able to locally refine the interface region and model the antibody in complex with NTD as Cα chains.

We compared the heavy and light chain epitope footprints on NTD for antibodies 4-18 (Figure 3B, right) and 2-17 (Figure 3C, right). Notably, the orientation of the heavy and light chains between 2-17 and 4-8 were rotated ~90 degrees from each other, indicating different modes of recognition and showing that they are of different classes.

We next asked whether other NTD-directed neutralizing antibodies derived from VH1-69 heavy chain might be members of the 2-17 or 4-8 classes. Analysis of light chains indicated antibodies 2-17 and COV2-2676, derived from genes KV3-15 and KV3-11, respectively, to be remarkably similar in their light chain CDR L3 regions, suggesting that 2-17 and COV2-2676 might be of the same class. Overall, we observed NTD-directed neutralizing antibodies from VH1-69 to form at least two classes, with similarity of light chains suggesting antibodies 2-17 and COV2-2676 might represent a reproducible class observed in two different donors.

Functional requirements for somatic hypermutation (SHM)

Sequence analyses showed that all NTD-directed antibodies accumulate somatic hypermutations (SHMs) in their paratope regions (Figures 1A, 2A, and 3A). To help understand characteristics of the antibody precursors, we reverted the paratope-region somatic hypermutations observed in seven NTD-directed antibodies (1-87, 1-68, 2-51, 4-18, 5-24, 4-8, and 2-17) to their respective germline residues. Overall, these germline-reverted antibodies showed substantially reduced binding affinities and neutralization potencies (Figure S6). For the VH1-24 multi-donor antibody class, antibodies 1-87, 1-68, and 2-51 shared two convergent SHMs (T30I and G55A/V) in heavy chain, reversion of which showed significantly (~4-20-fold) reduced binding affinity (Figures S6A and S6B). For antibodies 4-18 and 5-24, derived from VH3-30 and VH3-33, respectively, reversion of SHMs in combination in each antibody nearly abolished neutralization (Figure S6C). For the two VH1-69-derived antibodies 2-17 and 4-8, neutralization was improved by SHMs by ~20- and ~8-fold, respectively. Thus, all of the NTD-directed potently neutralizing antibodies we tested required affinity maturation to achieve high binding affinity and high potency. The VH3-30 and VH3-33 antibodies were more sensitive to SHMs than the antibodies derived from other VH genes. Nonetheless, antibodies corresponding to the initial recombinants, with reversion of all paratope SHMs in combination, could still bind to spike with apparent IgG K_Ds ~2–70 nM, suggesting that precursor B cells of the NTD antibodies are likely to be efficiently activated by spike binding. Gene-specific substitution profiles (Sheng et al., 2017) showed that the observed SHMs are each generated by the SHM machinery with high frequencies (Figures 1A, 2A, and 3A), suggesting

that requirements for SHM are unlikely to present a significant barrier to antibody development.

NTD-directed potently neutralizing antibodies have similar angles of approach

To gain an overall understanding of the angle of antibody approach to the spike by these NTD-directed potently neutralizing antibodies, we determined their angles of approach around a latitudinal axis to define freedom between viral and host cell membranes, and around a longitudinal axis to define freedom within the plane of the membrane. Relative to the viral spike, the latitudinal axis is perpendicular to the trimer axis, and the longitudinal axis is parallel to this axis. Latitudinal and longitudinal approach angles among the NTD-neutralizing antibodies were similar—with antibodies approaching spike with antigen-combining surface oriented toward the viral membrane (Figures 4A–4C).

We also analyzed the heavy-light chain orientations in the complexes with spike (Figure 4D). Here, the NTD-directed antibodies differed, with three of the antibodies, 4-18 from VH3-30 and 2-17 and 4-8 from VH1-69, showing heavy and light chain angles of approach that differed from the other five antibodies. Thus, while the heavy/light orientation relative to spike could differ substantially, lesser differences were observed in latitudinal and longitudinal angles of approach, with all NTD-neutralizing antibodies approaching spike from "above" with their antigen-binding surfaces oriented toward the viral membrane.

NTD-directed antibodies induce conformational changes in NTD and spike

To gain insight into the impact of antibody recognition on the conformation of NTD, we superimposed antibody-spike or antibody-NTD complexes onto the NTD domain and examined the structural alteration in NTD versus NTD in the ligand-free spike (PDB: 6ZGE), calculating the per-residue Cα movement between bound and ligand-free (Figure 5A), which ranged as high as 16–18 Å for most of the NTD-directed antibodies, though 4-8 (10.1 Å) and 5-24 (11.7 Å) were somewhat lower. The largest structural change occurred in the N3 β-hairpin, although the mobile N1 and N5 loops also showed large deviations (Figure 5B). In general, the regions of NTD that moved were contacted by antibody (Figure 5C), indicating that the conformational changes were a direct consequence of antibody binding. In addition to the conformational change induced in NTD, we observed other changes in spike. Notably, the 4-18 antibody-bound spike was substantially better ordered than the other NTD-bound spikes (achieving a nominal cryo-EM resolution of 2.97 Å, which was ~1 Å better than most of the other complexes). Examination of the 4-18 bound spike indicated almost 40° rotation in the central S2 triple helical bundle (Figure S4E).

Overall, binding of NTD-directed antibodies induced substantial structural rearrangements, not only in recognized loops but also of the N3 β-hairpin. The higher immunogenicity observed with flexible regions likely stems from increased accessibility due to lower glycan coverage as well as the ability of these regions to assume distinct conformations required for diverse antibodies to bind, with the recognized site on NTD apparently exemplifying this effect.
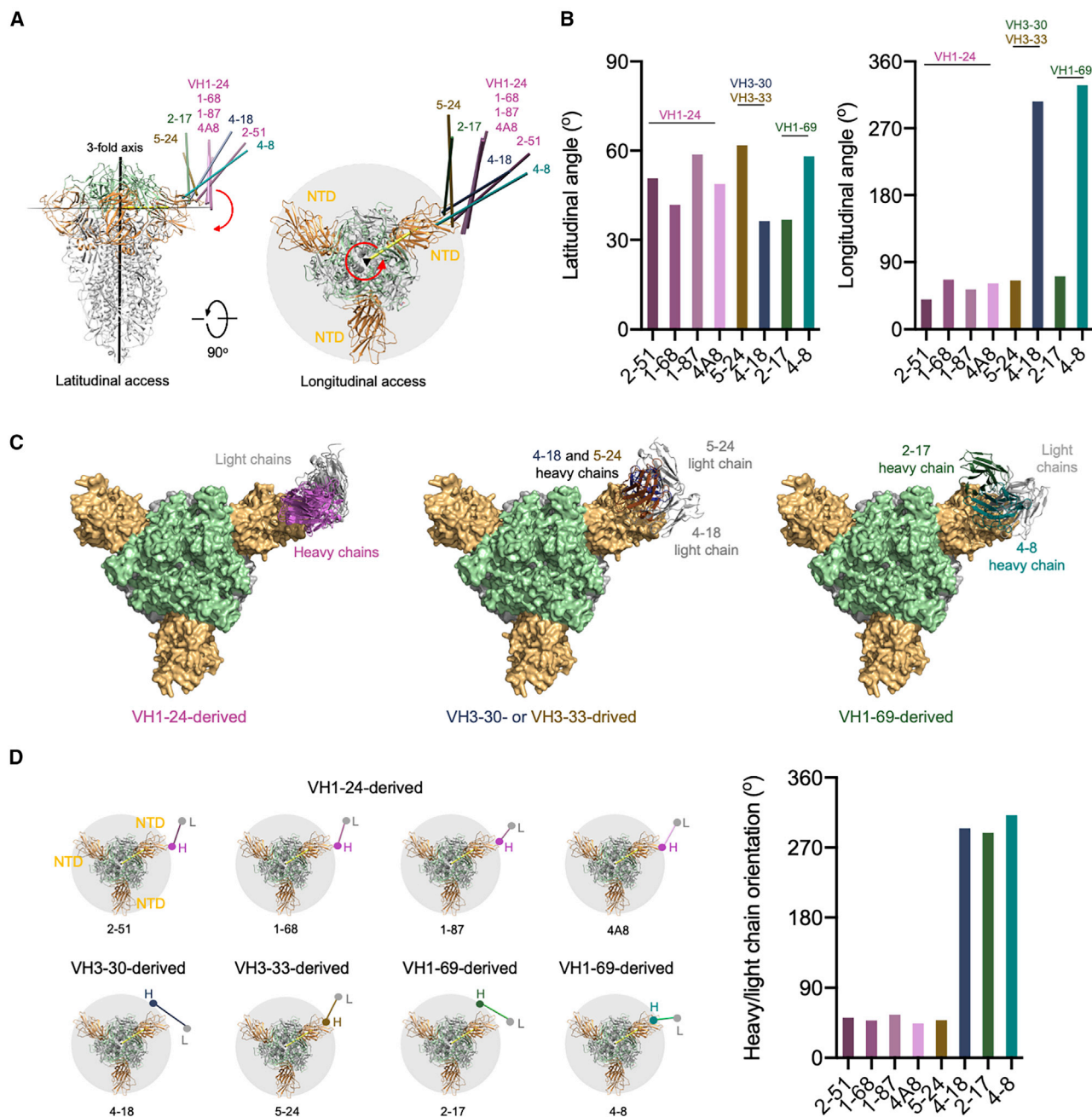
Figure 4. Angles of approach for NTD-directed neutralizing antibodies

(A) Overall approach of NTD-directed neutralizing antibodies to spike with angles defined with red arrows. The 3-fold axis is indicated by a black triangle. Antibodies are represented by long axes of the Fabs and colored by heavy chain colors defined in Figures 1, 2, and 3.

(B) Latitudinal and longitudinal angles of approach.

(C) Angles of recognition for antibodies grouped by VH gene. Notably, only those from VH1-24 show a consistent orientation.

(D) Heavy-light chain orientations show graphically (left) and quantitatively (right).

The NTD supersite

To define the spike surface recognized by potent NTD-directed neutralizing antibodies, we analyzed the epitopes for all eight of the NTD-directed neutralizing antibodies with defined structures: the seven described in this study as well as antibody 4A8, described previously (Table S3) (Chi et al., 2020). These ranged in potency from remarkably potent 2-17 and 2-51

antibodies with IC_{50} of 0.007 µg/mL to the neutralizing, but substantially less potent, 4A8 with IC_{50} of 0.39 µg/mL; all eight of these antibodies recognize overlapping epitopes on NTD (Figure 6A). Antigenic sites containing epitopes for genetically diverse antibodies have been widely denoted as antigenic "supersites" in prior studies involving influenza virus and HIV antibodies (Kong et al., 2013; Kumar et al., 2020; Lee and Wilson,
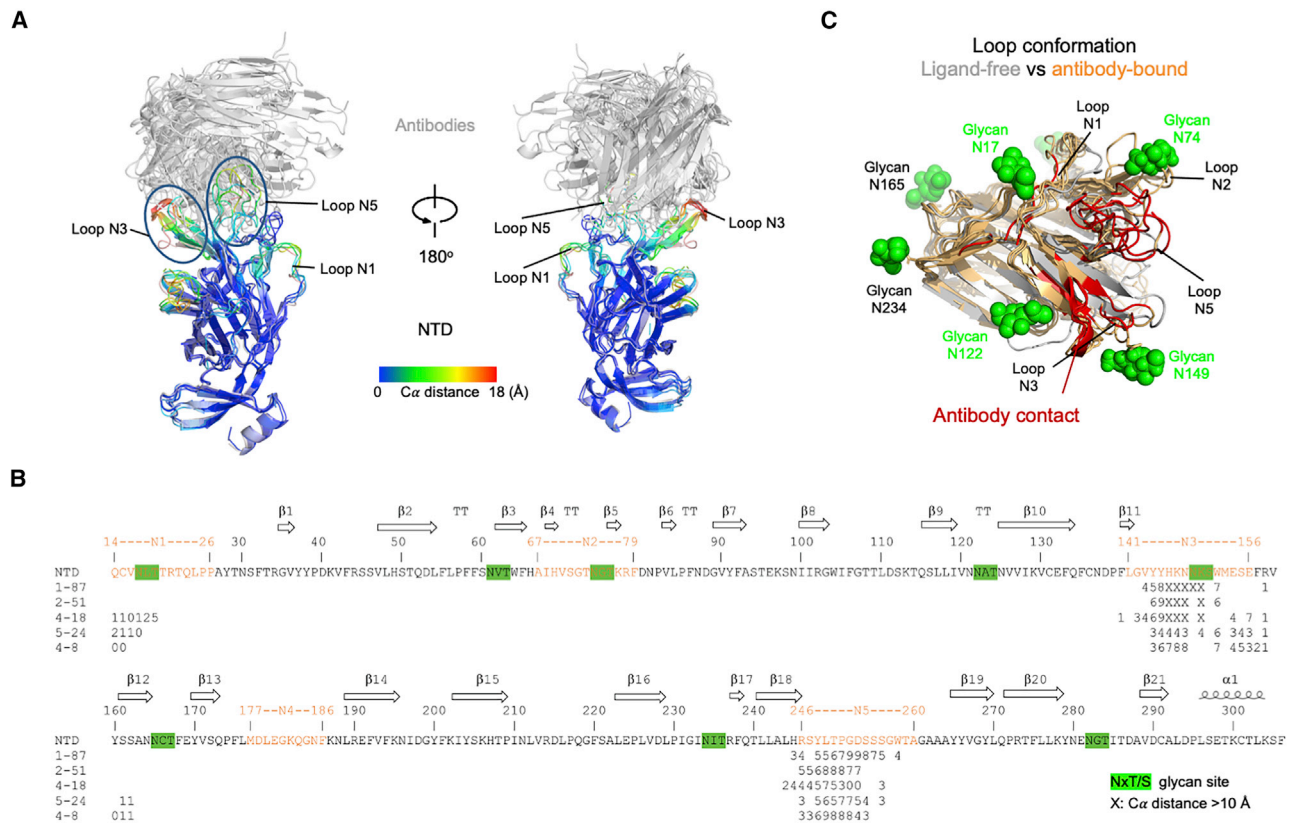
Figure 5. NTD-directed antibodies induce conformational changes in NTD and spike

(A) Conformational changes in NTD induced by binding of neutralizing antibodies. Antibody-bound NTDs are shown in cartoon representation and colored by per-residue Cα movements compared to unliganded NTD. Antibodies are shown in gray cartoon. Major NTD loops interacting with antibodies are labeled.

(B) Sequence of NTD highlighting antibody contact and conformational change. Epitope residues for each antibody are marked with a number representing Cα movements (Å) from unliganded NTD; the symbol "X" indicates movement 10 Å and above. Potential glycosylation sites on NTD are highlighted in green (distances are shown for antibodies with sufficiently resolved interfaces; antibody 2-17 was only at 4.4 Å, and the interface of antibody 1-68 showed extensive mobility.

(C) Epitope regions on NTD (red) and their conformational change. Glycans on NTD are shown as green spheres.

2015; Longo et al., 2016; Moyo et al., 2020; Zhou et al., 2015; Zhou et al., 2014); we define the spike surface recognized by at least two antibodies, from different classes, of these eight potent NTD-directed antibodies, as the NTD supersite (Figure 6B; Tables S4 and S5).

The NTD supersite was located at the periphery of the spike, distal from the 3-fold axis, and facing away from the viral membrane. This surface was surrounded by four glycans, *N*17, *N*74, *N*122, and *N*149, and nominally "glycan free," although molecular dynamics simulations with fully glycosylated spike indicated some glycan coverage, though less than adjacent regions more proximal to the spike 3-fold (Figure 6C).

To gain insight into the structural features of the NTD supersite, we first analyzed the distribution of epitopes versus potency, but did not observe substantial variation in potency over the NTD supersite (Figure 6D, left). In addition, we measured Fab affinity to spike (Table S6) but found no correlation with potency. Electrostatic surface analysis revealed the supersite to have strong positive electrostatic potential (Figure 6D, middle), while recognizing antibodies had complementary strong electronegative potential (Figure S7).

With respect to recognized conformation, we compared the ligand-free conformation of the supersite versus its antibody-bound conformation; the recognized β strands at the center of the epitope were displaced ~3 Å, with loops N1, N3, and N5 moving substantially more, up to 18 Å (Figure 6D, right). With respect to correlation with potency, we observed the magnitude of induced NTD conformational change to trend inversely with potency. This is not surprising in that the requirement for conformational change is likely to lower the energy of binding. Notably, antibodies that induced larger conformational changes were also more electronegative, potentially providing an explanation for the observation that increasing negative charge trended with reduced potency.

Overall, the NTD supersite comprised a structurally plastic surface, formed primarily by the N3 β-hairpin and including other flexible regions such as the N1 and N5 loops. This surface was also both glycan-free and highly electropositive—and facing away from the electronegative viral membrane.

NTD supersites in other betacoronaviruses

To understand the generality of the single-NTD supersite that we observe for SARS-CoV-2, we examined the recognition of
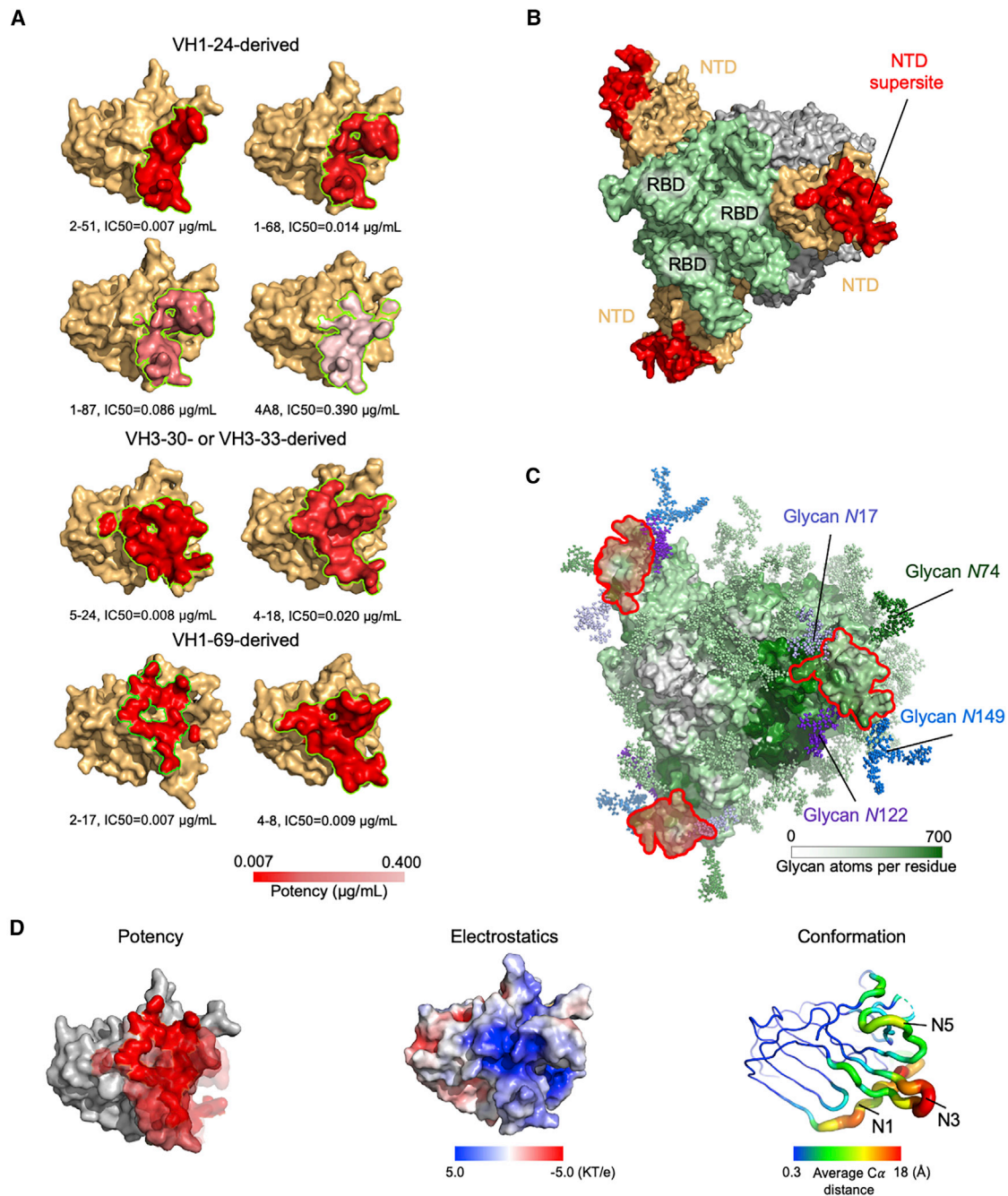
Figure 6. A structurally plastic antigenic supersite in the distal-loop region of NTD revealed by comparison of antibodies derived from the four multi-donor classes

(A) Epitopes of NTD-targeting antibodies colored by potency (cryo-EM structures were of sufficient resolution to define all epitopes, except for 2-17 and 1-68, which utilized polyAla-based template modeling and homology modeling, respectively). Epitope residues are listed in Table S3.

(B) The supersite of vulnerability on NTD. Supersite residues are listed in Table S5.

(C) Glycan coverage of the spike. The NTD supersite is surrounded by glycans at N17, N74, N122, and N149.

(D) NTD structural properties and antibody potency. Epitope surfaces of different antibodies were overlaid onto NTD with shades of red representing potency (left). Electrostatic potential on NTD (middle). Structural variation of NTD bound by NTD-directed antibodies (right).

See also Figures S1, S6, and S7, and Tables S3–S6.

NTD-directed neutralizing antibodies targeting other betacoronaviruses. Searches of the PDB found only two NTD-directed antibodies targeting other betacoronaviruses: these two antibodies,

G2 (Wang et al., 2018) and 7d10 (Zhou et al., 2019), both neutralized MERS and targeted overlapping glycan-free surfaces on NTD facing away from the viral membrane (Figure 7A). The
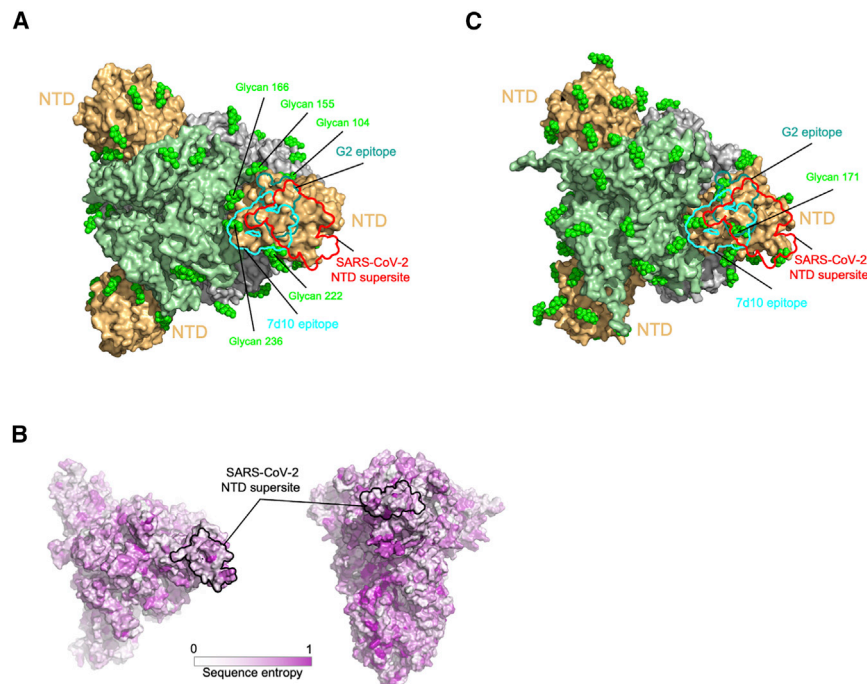
![CellPress logo]

Figure 7. NTD supersite on MERS betacoronaviruses
(A) Epitopes of MERS NTD antibodies target a site closer to the trimer axis. Borders of epitopes of antibody G2 and 7d10 are colored teal and cyan, respectively. SARS-CoV-2 NTD supersite is show as red boundary line. Glycans are shown as green spheres.
(B) Spike sequence entropy between betacoronaviruses.
(C) NTD of HKU1 spike is substantially glycosylated.

epitopes for both of these antibodies partially overlapped the analogous surface comprising the NTD supersite in SARS-CoV-2 but were more centrally located and more proximal to the spike 3-fold.

Quantification of the average number of proximal glycan atoms indicated lower glycan density over the NTD supersite than over the equivalent surfaces recognized by G2 and 7d10 antibodies. The epitopes recognized by these two antibodies also showed substantially less conformational mobility. Thus, potent NTD-directed neutralizing antibodies targeting SARS-CoV-2 preferentially recognized a less glycosylated, more flexible region than the analogous surfaces recognized by NTD-directed antibodies neutralizing MERS.

Since the MERS- and SARS-CoV-2-directed antibodies both targeted glycan-free sites on NTD facing away from the viral membrane, we sought to understand the properties of the analogous surfaces of other coronavirus spikes. We calculated the sequence divergence of other betacoronoviruses and mapped this to the NTD surface, which showed high diversity in sequence (Figure 7B). We modeled the sequence-predicted glycans on the HKU1 spike structure (PDB: 5I08) and examined the location of glycans on HKU1 NTD (Figure 7C). Notably, glycan *N*171 was observed to be directly the region of overlap between the equivalent positions of the SARS-CoV-2 supersite, 7d10 and G2 epitopes. Thus, the presence of glycans may impact the presence or absence of NTD sites of vulnerability in betacoronaviruses.

DISCUSSION

Antibodies directed to NTD and to RBD can neutralize with high potency (less than 0.01 μg/mL IC$_{50}$). While RBD shows many non-overlapping sites of vulnerability to antibody (Barnes et al., 2020a; Brouwer et al., 2020; Lv et al., 2020; Pinto et al., 2020; Yuan et al., 2020a), NTD appears to contain only a single site

of vulnerability to neutralization. As discussed above, one reason for this may be the high glycan density on NTD, with 8 *N*-linked glycans in ~300 residues, a density of one glycan per ~40 residues, and few glycan-free surfaces that can be easily recognized by the immune system. A second reason may be the restricted approach angle that we observed for all known NTD-directed neutralizing antibodies, including the seven reported here, which all approach spike from "above." We note in this context that competition analysis indicates other NTD-directed antibodies capable of recognizing spike and forming a separate competition group to be non-neutralizing (Liu et al., 2020a)—and the other large surface on NTD that is exposed on spike faces toward the viral membrane. This surface is mostly glycan free, and antibodies binding to it would be required to approach from "below." Thus, unlike RBD, where neutralizing antibodies appear to have diverse approach angles, the presence of only a single-NTD site of vulnerability may relate to the requirement to approach from above.

In addition to satisfying requirements stemming from the restricted approach angle, the higher relative prevalence of NTD-supersite-directed antibodies is likely to stem from increased immunogenicity due to both the lower relative glycan density of the supersite and the flexible nature of the N3 hairpin and N5 loop primary recognition regions, as well as their ability to assume distinct conformations that allow for recognition by diverse antibodies. In the case of the multi-donor VH1-24 antibody class, which arises from the most prevalent VH gene utilized (Figure S1A), two additional NTD-directed neutralizing class members have recently been identified: FC05 and CM25 (Voss et al., 2020; Wang et al., 2021). We found VH1-24 to be the most negatively charged human VH gene (Figure S5B). Such negative electrostatic potential complements the highly electropositive nature of the NTD supersite that we observe here (Figure 6D). Thus, multiple factors, including epitope glycosylation and flexibility, restrictions on approach angle, and paratope charge complementarity, can contribute to the prevalence of antibodies targeting the NTD supersite.

Although the approach to the spike from above observed for all NTD-directed neutralizing antibodies is consistent with a neutralization mechanism based on steric hindrance of spike

interaction with ACE2 receptor at the cell membrane, there is currently no evidence for competition between NTD-directed antibodies and ACE2 (Liu et al., 2020a). A plausible alternative model would be for antibody recognition of the NTD supersite to impede spike function in mediating fusion of virus and host cell membranes. Indeed, protease-resistance analysis of MERS spike in complex with MERS NTD-directed neutralizing antibody 7d10 showed that 7d10 binding prevented increased protease sensitivity associated with the prefusion-to-postfusion transition (Zhou et al., 2019). A conformational stabilization mechanism could also explain how an antibody that binds only one subunit per spike trimer could achieve effective neutralization. Further studies will be required to understand mechanisms of neutralization for antibodies that recognize the NTD supersite.

With respect to vaccine implications, our results clearly identify the NTD site of vulnerability most likely to elicit neutralizing antibodies. There are many ways that this information can be incorporated into vaccine design, including the inclusion of NTD along with RBD in vaccine formulations, the multivalent display of the NTD supersite on nanoparticle immunogens, and epitope-focusing through the creation of scaffolds displaying the N3 β-hairpin and other regions of recognized by NTD-directed neutralizing antibodies.

With respect to the therapeutic potential of NTD-directed antibodies, these target a site that is remote from those targeting RBD sites and thus should provide complementary neutralization to RBD-directed antibodies and require distinct escape pathways. The fact that all, or a great majority, of NTD-neutralizing antibodies target a single site, however, suggests there may be little utility to utilizing combinations of NTD-directed neutralizing antibodies.

Finally, new mutant SARS-CoV-2 strains, particularly those emerged in the UK and South Africa (strains B.1.1.7 and B.1.351, respectively), are concerning due to increased transmissibility, and these strains escape most NTD-directed neutralizing antibodies. B.1.1.7 includes NTD deletion mutations D69-70 and D144, and strain B.1.351 includes NTD mutations D242-244 and R246I. Consistent with our findings, the mutated positions including 144, 242-244, and 246 are all within the NTD supersite. While the deletion at 69-70 is outside of the supersite, it forms part of the hairpin N2 loop of NTD; its deletion could significantly impact the conformation of the NTD supersite. Notably, only three residues were shared among the eight NTD-directed neutralizing antibody epitopes analyzed here: Y144, R246, and L249 (Table S5). Interestingly, two of these three residues are the exact residues mutated in emerging variants of concern (Δ144 and R246I), and L249 is likely affected by Δ242-244. Thus, the flipside of a single supersite is that variation of the supersite may induce resistance against most of the antibodies targeting the site—and be selected for among emerging variants.

STAR★METHODS

Detailed methods are provided in the online version of this paper and include the following:

- KEY RESOURCES TABLE
- RESOURCE AVAILABILITY
  - ○ Lead contact
  - ○ Materials availability
  - ○ Data and code availability
- EXPERIMENTAL MODEL AND SUBJECT DETAILS
  - ○ Cell lines
- METHOD DETAILS
  - ○ Protein samples expression and purification
  - ○ Antibody mutagenesis
  - ○ Antibody Fab binding affinity measurement by surface plasmon resonance
  - ○ Full IgG binding affinity measurements by surface plasmon resonance
  - ○ Pseudoviruses neutralization assays
  - ○ Authentic SARS-CoV-2 microplate neutralization
  - ○ Antibody gene assignments and genetic analyses
  - ○ Cryo-EM samples preparation
  - ○ Cryo-EM data collection, processing and structure refinement
  - ○ X-ray crystallography sample preparation, data collection, structure solution and refinement
  - ○ Calculation of antibody angle of approach
  - ○ Glycan analysis
  - ○ Interface definition and net charge computation
  - ○ Cα distance calculation
  - ○ RMSD calculation
  - ○ Sequence entropy of betacoronavirus spike
- QUANTIFICATION AND STATISTICAL ANALYSIS

AUTHOR CONTRIBUTIONS

G.C. led the determination of five cryo-EM structures shown in Figures 1, 2, and 3; Y.G. provided sequence analyses defining classes in Figures 1, 2,

and 3; T.Z. led analysis for Figures 4, 5, 6, and 7; J.G. carried out map refinement and model building for 4-8 and 2-17 structures with spike; M.L. provided glycan-masking analysis for supersite, correlations for supersite properties, and threading of diverse spikes; M.R. led determination of one cryo-EM structure; E.R.R. led crystal structure determination of 2-51 with isolated NTD; J.Y. provided antibodies for structural analysis; F.B. provided spike, mutant spikes, and stabilized spikes; J.B. provided almost all Fabs; Y.H., L.L., M.S.N., and P.W. carried out antibody reversion analyses; Y.H. and M.S.N. performed authentic virus neutralization; P.S.K. determined SPR affinity measurements; R.R. assisted with glycan density calculations; A.S.O. provided spike; B.Z. provided antibodies; G.-Y.C. supervised informatics analysis and assisted with antibody structural threading and docking; D.D.H. supervised IgG production and reversion analysis; Z.S. supervised sequence analysis; P.D.K. supervised structural analyses; and L.S. supervised structural determinations and led the overall project.

REFERENCES

Adams, P.D., Gopal, K., Grosse-Kunstleve, R.W., Hung, L.W., Ioerger, T.R., McCoy, A.J., Moriarty, N.W., Pai, R.K., Read, R.J., Romo, T.D., et al. (2004). Recent developments in the PHENIX software for automated crystallographic structure determination. J. Synchrotron Radiat. 11, 53–55.

Adams, P.D., Afonine, P.V., Bunkóczi, G., Chen, V.B., Davis, I.W., Echols, N., Headd, J.J., Hung, L.W., Kapral, G.J., Grosse-Kunstleve, R.W., et al. (2010). PHENIX: a comprehensive Python-based system for macromolecular structure solution. Acta Crystallogr. D Biol. Crystallogr. 66, 213–221.

Barad, B.A., Echols, N., Wang, R.Y., Cheng, Y., DiMaio, F., Adams, P.D., and Fraser, J.S. (2015). EMRinger: side chain-directed model and map validation for 3D cryo-electron microscopy. Nat. Methods 12, 943–946.

Barnes, C.O., Jette, C.A., Abernathy, M.E., Dam, K.A., Esswein, S.R., Gristick, H.B., Malyutin, A.G., Sharaf, N.G., Huey-Tubman, K.E., Lee, Y.E., et al. (2020a). SARS-CoV-2 neutralizing antibody structures inform therapeutic strategies. Nature 588, 682–687.

Barnes, C.O., West, A.P., Jr., Huey-Tubman, K.E., Hoffmann, M.A.G., Sharaf, N.G., Hoffman, P.R., Koranda, N., Gristick, H.B., Gaebler, C., Muecksch, F., et al. (2020b). Structures of Human Antibodies Bound to SARS-CoV-2 Spike Reveal Common Epitopes and Recurrent Features of Antibodies. Cell 182, 828–842.e16.

Benton, D.J., Wrobel, A.G., Xu, P., Roustan, C., Martin, S.R., Rosenthal, P.B., Skehel, J.J., and Gamblin, S.J. (2020). Receptor binding and priming of the spike protein of SARS-CoV-2 for membrane fusion. Nature 588, 327–330.

Bepler, T., Morin, A., Rapp, M., Brasch, J., Shapiro, L., Noble, A.J., and Berger, B. (2019). Positive-unlabeled convolutional neural networks for particle picking in cryo-electron micrographs. Nat. Methods 16, 1153–1160.

Brochet, X., Lefranc, M.-P., and Giudicelli, V. (2008). IMGT/V-QUEST: the highly customized and integrated system for IG and TR standardized V-J and V-D-J sequence analysis. Nucleic Acids Res. 36, W503–W508.

Brouwer, P.J.M., Caniels, T.G., van der Straten, K., Snitselaar, J.L., Aldon, Y., Bangaru, S., Torres, J.L., Okba, N.M.A., Claireaux, M., Kerster, G., et al. (2020). Potent neutralizing antibodies from COVID-19 patients define multiple targets of vulnerability. Science 369, 643–650.

Burton, D.R., and Walker, L.M. (2020). Rational Vaccine Design in the Time of COVID-19. Cell Host Microbe 27, 695–698.

Callaway, E., Cyranoski, D., Mallapaty, S., Stoye, E., and Tollefson, J. (2020). The coronavirus pandemic in five powerful charts. Nature 579, 482–483.

Cao, Y., Su, B., Guo, X., Sun, W., Deng, Y., Bao, L., Zhu, Q., Zhang, X., Zheng, Y., Geng, C., et al. (2020). Potent neutralizing antibodies against SARS-CoV-2 identified by high-throughput single-cell sequencing of convalescent patients' B cells. Cell 182, 73–84.e16, https://doi.org/10.1016/j.cell.2020.1005.1025.

Casalino, L., Gaieb, Z., Goldsmith, J.A., Hjorth, C.K., Dommer, A.C., Harbison, A.M., Fogarty, C.A., Barros, E.P., Taylor, B.C., McLellan, J.S., et al. (2020). Beyond Shielding: The Roles of Glycans in the SARS-CoV-2 Spike Protein. ACS Cent. Sci. 6, 1722–1734.

Chen, Y., Lu, S., Jia, H., Deng, Y., Zhou, J., Huang, B., Yu, Y., Lan, J., Wang, W., Lou, Y., et al. (2017). A novel neutralizing monoclonal antibody targeting the N-terminal domain of the MERS-CoV spike protein. Emerg. Microbes Infect. 6, e60.

Chen, X., Li, R., Pan, Z., Qian, C., Yang, Y., You, R., Zhao, J., Liu, P., Gao, L., Li, Z., et al. (2020). Human monoclonal antibodies block the binding of SARS-CoV-2 spike protein to angiotensin converting enzyme 2 receptor. Cell. Mol. Immunol. 17, 647–649.

Chi, X., Yan, R., Zhang, J., Zhang, G., Zhang, Y., Hao, M., Zhang, Z., Fan, P., Dong, Y., Yang, Y., et al. (2020). A neutralizing human antibody binds to the N-terminal domain of the Spike protein of SARS-CoV-2. Science 369, 650–655.

Cucinotta, D., and Vanelli, M. (2020). WHO Declares COVID-19 a Pandemic. Acta Biomed. 91, 157–160.

Davis, I.W., Murray, L.W., Richardson, J.S., and Richardson, D.C. (2004). MOLPROBITY: structure validation and all-atom contact analysis for nucleic acids and their complexes. Nucleic Acids Res. 32, W615–W619.

Dong, E., Du, H., and Gardner, L. (2020). An interactive web-based dashboard to track COVID-19 in real time. Lancet Infect. Dis. 20, 533–534.

Dunbar, J., Krawczyk, K., Leem, J., Marks, C., Nowak, J., Regep, C., Georges, G., Kelm, S., Popovic, B., and Deane, C.M. (2016). SAbPred: a structure-based antibody prediction server. Nucleic Acids Res. 44 (W1), W474–W478.

Edgar, R.C. (2004). MUSCLE: multiple sequence alignment with high accuracy and high throughput. Nucleic Acids Res. 32, 1792–1797.

Emsley, P., and Cowtan, K. (2004). Coot: model-building tools for molecular graphics. Acta Crystallogr. D Biol. Crystallogr. 60, 2126–2132.

Evans, P.R., and Murshudov, G.N. (2013). How good are my data and what is the resolution? Acta Crystallogr. D Biol. Crystallogr. 69, 1204–1214.

Grant, B.J., Rodrigues, A.P., ElSawy, K.M., McCammon, J.A., and Caves, L.S. (2006). Bio3d: an R package for the comparative analysis of protein structures. Bioinformatics 22, 2695–2696.

Hansen, J., Baum, A., Pascal, K.E., Russo, V., Giordano, S., Wloga, E., Fulton, B.O., Yan, Y., Koon, K., Patel, K., et al. (2020). Studies in humanized mice and convalescent humans yield a SARS-CoV-2 antibody cocktail. Science 369, 1010–1014, https://doi.org/10.1126/science.abd0827.

Hsieh, C.L., Goldsmith, J.A., Schaub, J.M., DiVenere, A.M., Kuo, H.C., Javanmardi, K., Le, K.C., Wrapp, D., Lee, A.G., Liu, Y., et al. (2020). Structure-based design of prefusion-stabilized SARS-CoV-2 spikes. Science 369, 1501–1505.

Jo, S., Kim, T., Iyer, V.G., and Im, W. (2008). CHARMM-GUI: a web-based graphical user interface for CHARMM. J. Comput. Chem. 29, 1859–1865.

Joosten, R.P., Long, F., Murshudov, G.N., and Perrakis, A. (2014). The PDB_REDO server for macromolecular structure model optimization. IUCrJ 1, 213–220.

Ju, B., Zhang, Q., Ge, J., Wang, R., Sun, J., Ge, X., Yu, J., Shan, S., Zhou, B., Song, S., et al. (2020). Human neutralizing antibodies elicited by SARS-CoV-2 infection. Nature 584, 115–119, https://doi.org/10.1038/s41586-41020-42380-z.

Kabsch, W. (2010). Integration, scaling, space-group assignment and post-refinement. Acta Crystallogr. D Biol. Crystallogr. 66, 133–144.

Katoh, K., Misawa, K., Kuma, K., and Miyata, T. (2002). MAFFT: a novel method for rapid multiple sequence alignment based on fast Fourier transform. Nucleic Acids Res. 30, 3059–3066.

Kong, L., Lee, J.H., Doores, K.J., Murin, C.D., Julien, J.P., McBride, R., Liu, Y., Marozsan, A., Cupo, A., Klasse, P.J., et al. (2013). Supersite of immune

vulnerability on the glycosylated face of HIV-1 envelope glycoprotein gp120. Nat. Struct. Mol. Biol. *20*, 796–803.

Kreer, C., Zehner, M., Weber, T., Ercanoglu, M.S., Gieselmann, L., Rohde, C., Halwe, S., Korenkov, M., Schommers, P., Vanshylla, K., et al. (2020). Longitudinal Isolation of Potent Near-Germline SARS-CoV-2-Neutralizing Antibodies from COVID-19 Patients. Cell *182*, 1663–1673.

Krissinel, E., and Henrick, K. (2007). Inference of macromolecular assemblies from crystalline state. J. Mol. Biol. *372*, 774–797.

Kumar, S., Ju, B., Shapero, B., Lin, X., Ren, L., Zhang, L., Li, D., Zhou, Z., Feng, Y., Sou, C., et al. (2020). A V$_H$1-69 antibody lineage from an infected Chinese donor potently neutralizes HIV-1 by targeting the V3 glycan supersite. Sci. Adv. *6*, https://doi.org/10.1126/sciadv.abb1328.

Lee, P.S., and Wilson, I.A. (2015). Structural characterization of viral epitopes recognized by broadly cross-reactive antibodies. Curr. Top. Microbiol. Immunol. *386*, 323–341.

Lefranc, M.P. (2008). IMGT, the International ImMunoGeneTics Information System for Immunoinformatics : methods for querying IMGT databases, tools, and web resources in the context of immunoinformatics. Mol. Biotechnol. *40*, 101–111.

Liu, L., Wang, P., Nair, M.S., Yu, J., Rapp, M., Wang, Q., Luo, Y., Chan, J.F., Sahi, V., Figueroa, A., et al. (2020a). Potent neutralizing antibodies against multiple epitopes on SARS-CoV-2 spike. Nature *584*, 450–456.

Liu, X., Gao, F., Gou, L., Chen, Y., Gu, Y., Ao, L., Shen, H., Hu, Z., Guo, X., and Gao, W. (2020b). Neutralizing Antibodies Isolated by a site-directed Screening have Potent Protection on SARS-CoV-2 Infection. bioRxiv. https://doi.org/10.1101/2020.05.03.074914.

Longo, N.S., Sutton, M.S., Shiakolas, A.R., Guenaga, J., Jarosinski, M.C., Georgiev, I.S., McKee, K., Bailer, R.T., Louder, M.K., O'Dell, S., et al. (2016). Multiple Antibody Lineages in One Donor Target the Glycan-V3 Supersite of the HIV-1 Envelope Glycoprotein and Display a Preference for Quaternary Binding. J. Virol. *90*, 10574–10586.

Lv, Z., Deng, Y.Q., Ye, Q., Cao, L., Sun, C.Y., Fan, C., Huang, W., Sun, S., Sun, Y., Zhu, L., et al. (2020). Structural basis for neutralization of SARS-CoV-2 and SARS-CoV by a potent therapeutic antibody. Science *369*, 1505–1509.

McCoy, A.J. (2007). Solving structures of protein complexes by molecular replacement with Phaser. Acta Crystallogr. D Biol. Crystallogr. *63*, 32–41.

Mitternacht, S. (2016). FreeSASA: An open source C library for solvent accessible surface area calculations. F1000Res. *5*, 189.

Moyo, T., Kitchin, D., and Moore, P.L. (2020). Targeting the N332-supersite of the HIV-1 envelope for vaccine design. Expert Opin. Ther. Targets *24*, 499–509.

Pallesen, J., Wang, N., Corbett, K.S., Wrapp, D., Kirchdoerfer, R.N., Turner, H.L., Cottrell, C.A., Becker, M.M., Wang, L., Shi, W., et al. (2017). Immunogenicity and structures of a rationally designed prefusion MERS-CoV spike antigen. Proc. Natl. Acad. Sci. USA *114*, E7348–E7357.

Pettersen, E.F., Goddard, T.D., Huang, C.C., Couch, G.S., Greenblatt, D.M., Meng, E.C., and Ferrin, T.E. (2004). UCSF Chimera–a visualization system for exploratory research and analysis. J. Comput. Chem. *25*, 1605–1612.

Pettersen, E.F., Goddard, T.D., Huang, C.C., Meng, E.C., Couch, G.S., Croll, T.I., Morris, J.H., and Ferrin, T.E. (2021). UCSF ChimeraX: Structure visualization for researchers, educators, and developers. Protein Sci. *30*, 70–82.

Pinto, D., Park, Y.-J., Beltramello, M., Walls, A.C., Tortorici, M.A., Bianchi, S., Jaconi, S., Culap, K., Zatta, F., De Marco, A., et al. (2020). Cross-neutralization of SARS-CoV-2 by a human monoclonal SARS-CoV antibody. Nature *583*, 290–295.

Punjani, A., Rubinstein, J.L., Fleet, D.J., and Brubaker, M.A. (2017). cryoSPARC: algorithms for rapid unsupervised cryo-EM structure determination. Nat. Methods *14*, 290–296.

Robbiani, D.F., Gaebler, C., Muecksch, F., Lorenzi, J.C.C., Wang, Z., Cho, A., Agudelo, M., Barnes, C.O., Gazumyan, A., Finkin, S., et al. (2020). Convergent antibody responses to SARS-CoV-2 in convalescent individuals. Nature *584*, 437–442.

Rogers, T.F., Zhao, F., Huang, D., Beutler, N., Burns, A., He, W.T., Limbo, O., Smith, C., Song, G., Woehl, J., et al. (2020). Isolation of potent SARS-CoV-2

neutralizing antibodies and protection from disease in a small animal model. Science *369*, 956–963.

Scheres, S.H. (2012). RELION: implementation of a Bayesian approach to cryo-EM structure determination. J. Struct. Biol. *180*, 519–530.

Schramm, C.A., Sheng, Z., Zhang, Z., Mascola, J.R., Kwong, P.D., and Shapiro, L. (2016). SONAR: A High-Throughput Pipeline for Inferring Antibody Ontogenies from Longitudinal Sequencing of B Cell Transcripts. Front. Immunol. *7*, 372.

Sela-Culang, I., Kunik, V., and Ofran, Y. (2013). The structural basis of antibody-antigen recognition. Front. Immunol. *4*, 302.

Seydoux, E., Homad, L.J., MacCamy, A.J., Parks, K.R., Hurlburt, N.K., Jennewein, M.F., Akins, N.R., Stuart, A.B., Wan, Y.H., Feng, J., et al. (2020). Characterization of neutralizing antibodies from a SARS-CoV-2 infected individual. bioRxiv. https://doi.org/10.1101/2020.05.12.091298.

Sheng, Z., Schramm, C.A., Kong, R., NISC Comparative Sequencing Program, Mullikin, J.C., Mascola, J.R., Kwong, P.D., and Shapiro, L. (2017). Gene-Specific Substitution Profiles Describe the Types and Frequencies of Amino Acid Changes during Antibody Somatic Hypermutation. Front. Immunol. *8*, 537.

Suloway, C., Pulokas, J., Fellmann, D., Cheng, A., Guerra, F., Quispe, J., Stagg, S., Potter, C.S., and Carragher, B. (2005). Automated molecular microscopy: the new Leginon system. J. Struct. Biol. *151*, 41–60.

Tan, Y.Z., Baldwin, P.R., Davis, J.H., Williamson, J.R., Potter, C.S., Carragher, B., and Lyumkis, D. (2017). Addressing preferred specimen orientation in single-particle cryo-EM through tilting. Nat. Methods *14*, 793–796.

Voss, W.N., Hou, Y.J., Johnson, N.V., Kim, J.E., Delidakis, G., Horton, A.P., Bartzoka, F., Paresi, C.J., Tanno, Y., Abbasi, S.A., et al. (2020). Prevalent, protective, and convergent IgG recognition of SARS-CoV-2 non-RBD spike epitopes in COVID-19 convalescent plasma. bioRxiv. https://doi.org/10.1101/2020.12.20.423708.

Walls, A.C., Park, Y.J., Tortorici, M.A., Wall, A., McGuire, A.T., and Veesler, D. (2020). Structure, Function, and Antigenicity of the SARS-CoV-2 Spike Glycoprotein. Cell *181*, 281–292.e6.

Wang, L., Shi, W., Chappell, J.D., Joyce, M.G., Zhang, Y., Kanekiyo, M., Becker, M.M., van Doremalen, N., Fischer, R., Wang, N., et al. (2018). Importance of Neutralizing Monoclonal Antibodies Targeting Multiple Antigenic Sites on the Middle East Respiratory Syndrome Coronavirus Spike Glycoprotein To Avoid Neutralization Escape. J. Virol. *92*, 1–21.

Wang, C., Li, W., Drabek, D., Okba, N.M.A., van Haperen, R., Osterhaus, A.D.M.E., van Kuppeveld, F.J.M., Haagmans, B.L., Grosveld, F., and Bosch, B.J. (2020a). A human monoclonal antibody blocking SARS-CoV-2 infection. Nat. Commun. *11*, 2251.

Wang, Q., Zhang, Y., Wu, L., Niu, S., Song, C., Zhang, Z., Lu, G., Qiao, C., Hu, Y., Yuen, K.Y., et al. (2020b). Structural and Functional Basis of SARS-CoV-2 Entry by Using Human ACE2. Cell *181*, 894–904.e9.

Wang, N., Sun, Y., Feng, R., Wang, Y., Guo, Y., Zhang, L., Deng, Y.Q., Wang, L., Cui, Z., Cao, L., et al. (2021). Structure-based development of human antibody cocktails against SARS-CoV-2. Cell Res. *31*, 101–103.

Waterhouse, A., Bertoni, M., Bienert, S., Studer, G., Tauriello, G., Gumienny, R., Heer, F.T., de Beer, T.A.P., Rempfer, C., Bordoli, L., et al. (2018). SWISS-MODEL: homology modelling of protein structures and complexes. Nucleic Acids Res. *46* (W1), W296–W303.

Winn, M.D., Ballard, C.C., Cowtan, K.D., Dodson, E.J., Emsley, P., Evans, P.R., Keegan, R.M., Krissinel, E.B., Leslie, A.G., McCoy, A., et al. (2011). Overview of the CCP4 suite and current developments. Acta Crystallogr. D Biol. Crystallogr. *67*, 235–242.

Wrapp, D., De Vlieger, D., Corbett, K.S., Torres, G.M., Wang, N., Van Breedam, W., Roose, K., van Schie, L.; VIB-CMB COVID-19 Response Team, and Hoffmann, M., et al. (2020a). Structural Basis for Potent Neutralization of Betacoronaviruses by Single-Domain Camelid Antibodies. Cell *181*, 1004–1015.e15.

Wrapp, D., Wang, N., Corbett, K.S., Goldsmith, J.A., Hsieh, C.L., Abiona, O., Graham, B.S., and McLellan, J.S. (2020b). Cryo-EM structure of the 2019-nCoV spike in the prefusion conformation. Science *367*, 1260–1263.

Wrobel, A.G., Benton, D.J., Xu, P., Roustan, C., Martin, S.R., Rosenthal, P.B., Skehel, J.J., and Gamblin, S.J. (2020). SARS-CoV-2 and bat RaTG13 spike glycoprotein structures inform on virus evolution and furin-cleavage effects. Nat. Struct. Mol. Biol. *27*, 763–767, https://doi.org/10.1038/s41594-41020-40468-41597.

Wu, Y., Wang, F., Shen, C., Peng, W., Li, D., Zhao, C., Li, Z., Li, S., Bi, Y., Yang, Y., et al. (2020). A noncompeting pair of human neutralizing antibodies block COVID-19 virus binding to its receptor ACE2. Science *368*, 1274–1278.

Yan, R., Zhang, Y., Li, Y., Xia, L., Guo, Y., and Zhou, Q. (2020). Structural basis for the recognition of SARS-CoV-2 by full-length human ACE2. Science *367*, 1444–1448.

Ye, J., Ma, N., Madden, T.L., and Ostell, J.M. (2013). IgBLAST: an immunoglobulin variable domain sequence analysis tool. Nucleic Acids Res. *41*, W34–W40.

Yuan, M., Liu, H., Wu, N.C., Lee, C.D., Zhu, X., Zhao, F., Huang, D., Yu, W., Hua, Y., Tien, H., et al. (2020a). Structural basis of a shared antibody response to SARS-CoV-2. Science *369*, 1119–1123.

Yuan, M., Wu, N.C., Zhu, X., Lee, C.D., So, R.T.Y., Lv, H., Mok, C.K.P., and Wilson, I.A. (2020b). A highly conserved cryptic epitope in the receptor binding domains of SARS-CoV-2 and SARS-CoV. Science *368*, 630–633.

Zeng, X., Li, L., Lin, J., Li, X., Liu, B., Kong, Y., Zeng, S., Du, J., Xiao, H., Zhang, T., et al. (2020). Isolation of a human monoclonal antibody specific for the receptor binding domain of SARS-CoV-2 using a competitive phage biopanning strategy. Antibody Therapeutics *3*, 95–100.

Zhou, T., Zhu, J., Yang, Y., Gorman, J., Ofek, G., Srivatsan, S., Druz, A., Lees, C.R., Lu, G., Soto, C., et al. (2014). Transplanting supersites of HIV-1 vulnerability. PLoS ONE *9*, e99881.

Zhou, T., Lynch, R.M., Chen, L., Acharya, P., Wu, X., Doria-Rose, N.A., Joyce, M.G., Lingwood, D., Soto, C., Bailer, R.T., et al.; NISC Comparative Sequencing Program (2015). Structural Repertoire of HIV-1-Neutralizing Antibodies Targeting the CD4 Supersite in 14 Donors. Cell *161*, 1280–1292.

Zhou, H., Chen, Y., Zhang, S., Niu, P., Qin, K., Jia, W., Huang, B., Zhang, S., Lan, J., Zhang, L., et al. (2019). Structural definition of a neutralization epitope on the N-terminal domain of MERS-CoV spike glycoprotein. Nat. Commun. *10*, 3068.

Zhou, T., Tsybovsky, Y., Gorman, J., Rapp, M., Cerutti, G., Chuang, G.Y., Katsamba, P.S., Sampson, J.M., Schon, A., Bimela, J., et al. (2020). Cryo-EM Structures of SARS-CoV-2 Spike without and with ACE2 Reveal a pH-Dependent Switch to Mediate Endosomal Positioning of Receptor-Binding Domains. Cell Host Microbe *28*, 867–879.e5.

Zost, S.J., Gilchuk, P., Chen, R.E., Case, J.B., Reidy, J.X., Trivette, A., Nargi, R.S., Sutton, R.E., Suryadevara, N., Chen, E.C., et al. (2020). Rapid isolation and profiling of a diverse panel of human monoclonal antibodies targeting the SARS-CoV-2 spike protein. Nat. Med. *26*, 1422–1427.

STAR★METHODS

KEY RESOURCES TABLE

REAGENT or RESOURCE	SOURCE	IDENTIFIER
Antibodies		
1-68	Liu et al., 2020a	N/A
1-87	Liu et al., 2020a	N/A
2-17	Liu et al., 2020a	N/A
2-51	Liu et al., 2020a	N/A
4-8	Liu et al., 2020a	N/A
4-18	Liu et al., 2020a	N/A
5-24	Liu et al., 2020a	N/A
4A8	Chi et al., 2020	N/A
Bacterial and virus strains		
VSV-G pseudo-typed ΔG-luciferase	Kerafast	Cat# EH1020-PM
Chemicals, peptides, and recombinant proteins		
SARS-CoV-2 spike protein	Wrapp et al., 2020b	N/A
Polyethylenimine	Polysciences	Cat# 24765-2
Freestyle 293 Expression Media	Thermo Scientific	Cat# 12338-026
Expi293 Expression Medium	Thermo Scientific	Cat# A14635
Dulbecco's Modified Eagle Medium	ATCC	Cat# 30-2002
Fetal Bovine Serum, heat inactivated	Thermo Scientific	Cat# 16140071
Opti-MEM™ Reduced Serum Media	Thermo Scientific	Cat# 31985-070
IMAC Sepharose 6 Fast Flow	GE Healthcare	Cat# 17092109
Tris Base	Thermo Scientific	Cat# BP152-5
Sodium Chloride	Thermo Scientific	Cat# S271-10
Imidazole	ACROS	Cat# 301870025
Series S CM5 chip	Cytiva	Cat# BR100530
HEPES	Sigma	Cat# H3375
Sodium Chloride	Thermo Scientific	Cat# S271-10
Tween-20	Sigma	Cat# P7949
BSA	Sigma	Cat# A7906
His Capture kit	Cytiva	Cat# 28995056
Phosphoric acid	Sigma	Cat# 345245
Critical commercial assays		
FuGENE 6	Promega	Cat# E2691
Strep-Tactin XT Superflow 50%	Zymo research	Cat#P2004-1-5
Sensor Chip CM5	Cytiva	Cat#BR100030
His Capture Kit	Cytiva	Cat#28995056
Glycine 1.5	Cytiva	Cat# BR100354
HBS-EP+ Buffer	Cytiva	Cat# BR100826
Spin Miniprep Kit	QIAGEN	Cat# 27106
Hispeed Plasmid Maxi Kit	QIAGEN	Cat# 12663
HisTrap Fast Flow	GE Healthcare	Cat# 17-0921-09
Superdex 200 Increase 10/300 GL	Cytiva	Cat# 28990945
HRV3C protease	Thermo Scientific	Cat# PI88946
Pierce™ Fab Preparation Kit	Thermo Scientific	Cat# 44985
EndoHf	NEB	Cat# P0703S
Tris Base	Thermo Scientific	Cat# BP152-10

(Continued on next page)

Continued

REAGENT or RESOURCE	SOURCE	IDENTIFIER
Calcium acetate	Sigma	Cat# 114460-21-8
Sodium Cacodylate	Hampton research	Cat# HR2-575
Glycerol	Hampton research	Cat# HR2-623
PEG 8000	Sigma	Cat# 25322-68-3
Experimental models: Cell lines		
Vero E6	ATCC	Cat# CRL-1586
HEK293T/17	ATCC	Cat# CRL-11268
FreeStyle 293-F	Thermo Scientific	Cat# R79007
Expi293F Cells	Thermo Scientific	Cat# A14635
HEK293S GnTI-	ATCC	Cat# CRL-3022
I1 mouse hybridoma	ATCC	Cat# CRL-2700
Recombinant DNA		
pCMV3-SARS-CoV-2-spike	Dr. Peihui Wang, Shandong University, China	N/A
pα-H vector	Laboratory of Daniel Leahy	N/A
pVRC8400 vector	https://www.addgene.org	Cat#63160
Deposited data		
Crystallographic structure of neutralizing antibody 2-51 in complex with SARS-CoV-2 spike N-terminal domain (NTD)	This study	PDB: 7L2C
Cryo-EM structure of NTD-directed neutralizing antibody 1-87 in complex with prefusion SARS-CoV-2 spike glycoprotein	This study	PDB: 7L2D EMDB: EMD-23125
Cryo-EM structure of NTD-directed neutralizing antibody 4-18 in complex with prefusion SARS-CoV-2 spike glycoprotein	This study	PDB: 7L2E EMDB: EMD-23126
Cryo-EM structure of NTD-directed neutralizing antibody 5-24 in complex with prefusion SARS-CoV-2 spike glycoprotein	This study	PDB: 7L2F EMDB: EMD-23127
Cryo-EM structure of NTD-directed neutralizing antibody 4-8 in complex with prefusion SARS-CoV-2 spike glycoprotein	This study	PDB: 7LQV EMDB: EMD-23489
Cryo-EM structure of NTD-directed neutralizing antibody 2-17 in complex with prefusion SARS-CoV-2 spike glycoprotein	This study	PDB: 7LQW EMDB: EMD-23490
Cryo-EM map of NTD-directed neutralizing antibody 1-68 in complex with prefusion SARS-CoV-2 spike glycoprotein	This study	EMDB: EMD-23150
Cryo-EM map of NTD-directed neutralizing antibody 2-51 in complex with prefusion SARS-CoV-2 spike glycoprotein	This study	EMDB: EMD-23151
Software and algorithms		
AIMLESS	Evans and Murshudov, 2013	https://www.mrc-lmb.cam.ac.uk/harry/pre/aimless.html
CCP4	Winn et al., 2011	https://www.ccp4.ac.uk
Coot	Emsley and Cowtan, 2004	https://www2.mrc-lmb.cam.ac.uk/personal/pemsley/coot
cryoSPARC	Punjani et al., 2017	https://cryosparc.com
Leginon	Suloway et al., 2005	https://sbgrid.org/software/titles/leginon
Molprobity	Davis et al., 2004	http://molprobity.biochem.duke.edu
Phaser	McCoy, 2007	https://www.phenix-online.org/documentation/reference/phaser.html

Continued

REAGENT or RESOURCE	SOURCE	IDENTIFIER
Phenix	Adams et al., 2010	https://www.phenix-online.org
The PyMOL Molecular Graphics System, Version 2.0	Schrödinger, LLC	https://pymol.org/2/support.html#page-top
SAbPred	Dunbar et al., 2016	http://opig.stats.ox.ac.uk/webapps/newsabdab/sabpred
UCSF Chimera	Pettersen et al., 2004	https://www.cgl.ucsf.edu/chimera/
UCSF Chimera X	Pettersen et al., 2021	https://www.cgl.ucsf.edu/chimerax/
XDS	Kabsch, 2010	https://xds.mr.mpg.de/
GraphPad Prism Software	GraphPad Prism Software, Inc.	N/A
PDBePISA	Krissinel and Henrick, 2007	https://www.ebi.ac.uk/pdbe/pisa/
Scrubber 2.0	BioLogic Software	http://www.biologic.com.au/scrubber.html
The PyMol Molecular Graphics System, v1.8.6	Schrödinger, LLC	https://pymol.org/2/
IgBLAST-1.16	Ye et al., 2013	https://www.ncbi.nlm.nih.gov/igblast/
IMGT	Schramm et al., 2016	http://www.imgt.org/
MUSCLE v3.8.31	Edgar, 2004	https://www.drive5.com/muscle/manual/install.html
SONAR v2.0	Schramm et al., 2016	https://github.com/scharch/sonar/
Python v3.8.3		https://www.python.org/
The R Project for Statistical Computing		https://www.r-project.org/
R bio3d package	Grant et al., 2006	http://thegrantlab.org/bio3d/
MAFFT	Katoh et al., 2002	https://mafft.cbrc.jp/alignment/software/
FreeSASA v2.0.3	Mitternacht, 2016	https://freesasa.github.io/

RESOURCE AVAILABILITY

Lead contact
Further information and requests for resources and reagents should be directed to and will be fulfilled by the Lead Contact, Lawrence Shapiro (lss8@columbia.edu).

Materials availability
Expression plasmids generated in this study for expressing SARS-CoV-2 proteins and antibody mutants will be shared upon request.

Data and code availability
The cryo-EM structures and the crystallographic structure are in the process of being deposited to the Electron Microscopy Data Bank (EMDB) and the Protein Data Bank (RCSB PDB).

Cryo-EM structural models and maps of NTD-directed antibodies in complex with SARS-CoV-2 spike have been deposited in the PDB and EMDB for antibodies 1-87 (PDB:7L2D, EMDB: EMD-23125), 2-17 (PDB: 7LQW, EMDB: EMD-23490), 4-8 (PDB: 7LQV, EMDB: EMD-23489), 4-18 (PDB:7L2E, EMDB: EMD-23126) and 5-24 (PDB: 7L2F, EMDB: EMD-23127); cryo-EM maps have been deposited for antibodies 1-68 (EMDB: EMD-23150) and 2-51 (EMDB: EMD-231251). The crystallographic structure of antibody 2-51 in complex with SARS-CoV-2 spike NTD has been deposited in the PDB with accession code 7L2C.

EXPERIMENTAL MODEL AND SUBJECT DETAILS

Cell lines
FreeStyle 293-F (cat# R79007), Expi293F cells (cat# A14635) were from Thermo Fisher Scientific. HEK293S GnTI- (cat# CRL-3022), HEK293T/17 (cat# CRL-11268), I1 mouse hybridoma (cat# CRL-2700) and Vero E6 cells (cat# CRL-1586) were from ATCC.

FreeStyle 293-F cells and were cultured in serum-free FreeStyle 293 Expression Medium (GIBCO, cat# 12338026) at 37°C, 10% CO_2, 115 rpm. HEK293S GnTI- cells were cultured in FreeStyle 293 Expression Medium at 37°C, 10% CO_2, 115 rpm. Expi293F cells were cultured in Expi293 Expression Medium (GIBCO, cat# A14635) at 37°C, 8% CO_2, 125 rpm. HEK293T/17 cells and Vero E6 cells were cultured in 10% Fetal Bovine Serum (FBS, GIBCO cat# 16140071) supplemented Dulbecco's Modified Eagle Medium (DMEM, ATCC cat# 30-2002) at 37°C, 5% CO_2. Cell lines were not specifically authenticated.

METHOD DETAILS

Protein samples expression and purification

The SARS-CoV-2 S2P and HexaPro spike variant constructs were produced as described in Wrapp et al., 2020b and in Hsieh et al., 2020 respectively. They were expressed in Human Embryonic Kidney (HEK) Freestyle 293-F cells (Invitrogen) in suspension culture using serum-free media (Invitrogen) and transfected into HEK293 cells using polyethyleneimine (Polysciences). Cell growths were harvested four days after transfection, and the secreted proteins were purified from supernatant by nickel affinity chromatography using Ni-NTA IMAC Sepharose 6 Fast Flow resin (GE Healthcare) followed by size exclusion chromatography on a Superdex 200 column (GE Healthcare) in 10 mM Tris, 150 mM NaCl, pH 7.4.

The N-terminal domain of SARS-CoV-2 spike (NTD, residues 1-330) was cloned into the pVRC-8400 mammalian expression plasmid, with a C-terminal 6X-His-tag cleavable by HRV-3C protease. The NTD construct was transiently transfected into HEK293 GnTI- cells suspension culture in serum-free media using polyethyleneimine. Four days after transfection, the secreted protein was purified using Ni-NTA IMAC Sepharose 6 Fast Flow resin followed by size exclusion chromatography on a Superdex 200 column in 10 mM Tris, 150 mM NaCl, pH 7.4. Fractions containing NTD were combined and 1% (w/w) HRV-3C protease (Thermo fisher) was added to remove the C-terminal His-tag, followed by incubation for 24 h at 4°C. Inverse IMAC using Ni-NTA resin was then performed to purify NTD from the His-tag and residual uncleaved protein. Enzymatic deglycosylation of NTD was carried out by adding 2.5 μL Endo Hf (NEB) per 20 μg of NTD and incubating for 24 h at 25°C; a second round of SEC was performed to remove excess Endo Hf and to exchange buffer in 10 mM Tris, 150 mM NaCl, pH 7.4. Protein purity was analyzed by SDS-PAGE at every step.

NTD-directed monoclonal antibodies 1-68, 1-87, 2-17, 2-51, 4-8, 4-18 and 5-24 were expressed and purified as described in (Liu et al., 2020a). Fabs fragments were produced by digestion of IgGs with immobilized papain at 37°C for 3 h in 50 mM phosphate buffer, 120 mM NaCl, 30 mM cysteine, 1 mM EDTA, pH 7. The resulting Fabs were either purified from Fc by affinity chromatography on protein A (1-68, 1-87, 2-17, 2-51 and 4-8) or used as Fab/Fc mixture (4-18 and 5-24). Fab purity was analyzed by SDS-PAGE; all Fabs were buffer-exchanged into 10 mM Tris, 150 mM, pH 7.4 for crystallization and cryo-EM experiments.

Antibody mutagenesis

For each antibody, variable genes were optimized for human cell expression and synthesized by GenScript. VH and VL were inserted separately into plasmids (gWiz or pcDNA3.4) that encoding the constant region for heavy chain and light chain. Monoclonal antibodies were expressed in Expi293F (ThermoFisher, A14527) by co-transfection heavy chain and light chain expressing plasmids using polyethylenimine (PEI, Linear, MV~25,000, Polysciences, Inc. Cat. No. 23966) and culture in 37°C degree shaker at 125 rpm and 8% CO_2. Supernatants were collected on day 5, antibodies were purified by rProtein A Sepharose (GE, 17-1279-01) affinity chromatography.

Antibody gene mutations were introduced by QuikChange II site directed mutagenesis kit (Agilent, Cat. No. 200524).

Antibody Fab binding affinity measurement by surface plasmon resonance

SPR binding assays for Fabs were performed using a Biacore T200 biosensor, equipped with a Series S CM5 chip, in a running buffer of 10 mM HEPES pH 7.4, 150 mM NaCl, 0.1 mg/mL BSA and 0.01% (v/v) Tween-20 at 25°C.

HexaPro Spike was captured through its C-terminal his-tag over an anti-his antibody surface. These surfaces were generated using the His-capture kit (Cytiva, MA) according to the instructions of the manufacturer, resulting in approximately 10,000 RU of anti-his antibody over each surface. HexaPro was captured over a single flow cell at a capture level of 500-800RU with Fabs with higher KDs (2-17 and 4-18) requiring higher capture levels. An anti-his antibody surface was used as a reference flow cell to remove bulk shift changes from the binding signal.

Fabs were tested using a three-fold dilution series ranging from 2.96-240 nM, except for Fabs 4-18 and 2-17, which were analyzed at concentrations of 8.88-720 nM. The association and dissociation rates were each monitored for 120 s and 600 s respectively, at 50 μL/min. The bound HexaPro/Fab complex was regenerated from the anti-his antibody surface using a 10 s pulse of 15 mM H_3PO_4 at a flow rate of 100 μL/min, followed by a 60 s buffer wash at the same flow rate. Each Fab was tested in order of increasing protein concentration, in duplicate. Blank buffer cycles were performed by injecting running buffer instead of Fab to remove systematic noise from the binding signal. The data was processed and fit to 1:1 single cycle model using the Scrubber 2.0 (BioLogic Software). For each parameter reported, the number in brackets represents the error of the fit in the last significant figure.

Full IgG binding affinity measurements by surface plasmon resonance

The mammalian expression vector that encodes the ectodomain of the SARS-CoV-2 S trimer for full IgG binding affinity measurement was kindly provided by Dr. Jason McLellan (Wrapp et al., 2020b). SARS-CoV-2 S trimer expression vector was transiently transfected into Expi293 cells using 1 mg/mL of polyethylenimine (Polysciences). Five days post transfection, the S trimer was purified using Strep-Tactin XT Resin (Zymo Research).

The binding affinities of full IgG antibodies to SARS-CoV-2 spike protein were determined using surface plasmon resonance (SPR) and a BIAcore T200 instrument (GE Healthcare) at 25°C. The anti-his antibody was first immobilized onto two different flow cells of a CM5 sensorchip (BR100030, Cytiva) surface using the His Capture Kit (28995056, Cytiva) according to the manufacturer's protocol. The His-tagged SARS-CoV-2 spike protein was then injected and captured on flow cells 2. Flow cells 1 was used as the negative control. A three-fold dilution series of antibodies with concentrations ranging from 300 nM to 1.2 nM were injected over the sensor

surface for 30 s at a flow rate of 10 μL/minute. The dissociation was monitored for 300 s and the surface was regenerated with 10 mM Glycine pH 1.5 (BR100354, Cytiva). The running and sample buffer is 10 mM HEPES pH 7.4, 150 mM NaCl, 3 mM EDTA, 0.05% P-20 (HBS-EP+ buffer, BR100826, Cytiva). The resulting data were fit to a 1:1 binding model using Biacore Evaluation Software and were plotted using Graphpad.

Pseudoviruses neutralization assays

Recombinant Indiana VSV (rVSV) expressing SARS-CoV-2 spikes were generated as previously described. HEK293T cells were grown to 80% confluency before transfection with pCMV3-SARS-CoV-2-spike (kindly provided by Dr. Peihui Wang, Shandong University, China) using FuGENE 6 (Promega). Cells were cultured overnight at 37°C with 5% CO_2. The next day, medium was removed and VSV-G pseudo-typed ΔG-luciferase (G*ΔG-luciferase, Kerafast) was used to infect the cells in DMEM at a MOI of 3 for 1 h before washing the cells with 1X DPBS three times. DMEM supplemented with anti-VSV-G antibody (I1, mouse hybridoma supernatant from CRL-2700; ATCC) was added to the infected cells and they were cultured overnight as described above. The next day, the supernatant was harvested and clarified by centrifugation at 300 g for 10 min and aliquots stored at −80°C.

Neutralization assays were performed by incubating pseudoviruses with serial dilutions antibodies, and scored by the reduction in luciferase gene expression. In brief, Vero E6 cells were seeded in a 96-well plate at a concentration of 2×10^4 cells per well. Pseudoviruses were incubated the next day with serial dilutions of the test samples in triplicate for 30 min at 37°C. The mixture was added to cultured cells and incubated for an additional 24 h. The luminescence was measured by Britelite plus Reporter Gene Assay System (PerkinElmer). IC_{50} was defined as the dilution at which the relative light units were reduced by 50% compared with the virus control wells (virus + cells) after subtraction of the background in the control groups with cells only. The IC_{50} values were calculated using non-linear regression in GraphPad Prism.

Authentic SARS-CoV-2 microplate neutralization

An end-point dilution assay in a 96-well plate format was performed to measure the neutralization activity of purified mAbs. In brief, each antibody was serially diluted (5-fold dilutions) starting at 50 μg/mL. Triplicates of each mAb dilution were incubated with SARS-CoV-2 at an MOI of 0.1 in EMEM with 7.5% inactivated fetal calf serum (FCS) for 1 h at 37°C. Post incubation, the virus-antibody mixture was transferred onto a monolayer of Vero E6 cells grown overnight. The cells were incubated with the mixture for 70 h. Cytopathic effect (CPE) of viral infection was visually scored for each well in a blinded fashion by two independent observers. The results were then converted into percentage neutralization at a given mAb concentration, and the averages ± SEM were plotted using a five-parameter dose-response curve in GraphPad Prism v8.0.

Antibody gene assignments and genetic analyses

The 17 SARS-COV-2 neutralizing antibodies were collected from seven publications. We annotated these antibodies using IgBLAST-1.16.0 with the default parameters (Ye et al., 2013). For antibodies which have cDNA sequences deposited, the V and J genes were assigned using SONAR version 2.0 (https://github.com/scharch/sonar/) with germline gene database from IMGT (Lefranc, 2008; Schramm et al., 2016). For each antibody, the N-addition, D gene, and P-addition regions were annotated by IMGT V-QUEST (Brochet et al., 2008). To identify somatic hypermutations, each antibody sequence was aligned to the assigned germline gene using MUSCLE v3.8.31 (Edgar, 2004). Somatic hypermutations were identified from the alignment. In addition, the analysis of single cell antibody repertoire sequencing data of SARS-CoV-2 patient 2 from (Liu et al., 2020a), showed that 29 of the 38 unique transcripts assigned to IGLV2-14*01 share nucleotide mutations G156T and T165G. These mutations lead to amino acid mutations E50D and N53K. Both nucleotide mutations are also observed in 82 of 90 unique IGLV2-14 transcripts from patient 1 of the same study. Because these transcripts having different VJ recombination and paired with different heavy chain genes, the chances that the two convergent mutations are the results of somatic hypermutation are very low. Thus, we suspect that both donors contain a new IGLV2-14 gene allele (IGLV2-14*0X), which was deposited to European Nucleotide Archive (ENA) with project accession numbers: PRJEB31020. Light chain of 1-87 was assigned to the IGLV2-14*0X allele.

Cryo-EM samples preparation

Samples for cryo-EM grids preparation were produced by mixing purified SARS-CoV-2 S2P spike (final trimer concentration of 0.33 mg/mL) with NTD-directed Fabs in a 1:9 molar ratio, followed by incubation on ice for 1 h. The final buffer for 1-87, 4-18 and 5-24 complexes was 10 mM sodium acetate, 150 mM NaCl, pH 4.5; the final buffer for 1-68, 2-17, 2-51 and 4-8 complexes was 10 mM sodium acetate, 150 mM NaCl, pH 5.5. n-Dodecyl β-D-maltoside (DDM) at a final concentration of 0.005% (w/v) was added to the mixtures to prevent aggregation during vitrification. Cryo-EM grids were prepared by applying 2 μL of sample to a freshly glow-discharged carbon-coated copper grid (CF 1.2/1.3 300 mesh); the sample was vitrified in liquid ethane using a Vitrobot Mark IV with a wait time of 30 s and a blot time of 3 s.

Cryo-EM data collection, processing and structure refinement

Cryo-EM data were collected using the Leginon software (Suloway et al., 2005) installed on a Titan Krios electron microscope operating at 300 kV, equipped with a Gatan K3-BioQuantum direct detection device. The total dose was fractionated for 3 s over 60 raw frames or 2 s over 40 raw frames. Motion correction, CTF estimation, particle extraction, 2D classification, *ab initio* model generation, 3D refinements and local resolution estimation for all datasets were carried out in cryoSPARC 2.15 (Punjani et al., 2017); particles

were picked using Topaz (Bepler et al., 2019). Symmetry expansion and focused classification in RELION 3.1 (Scheres, 2012) was used for S2P spike complex with 2-51. The particle orientation distribution was assessed by angular distribution plots for all EM structures. Whenever a preferred orientation issue was identified, we calculated the sphericity values and the Fourier shell correlation (FSC) curves using the 3D FSC Processing Server (Tan et al., 2017).The interface between NTD and the Fab was locally refined by using a mask that included NTD and the variable domains of the Fab; symmetry-expanded particles in C3 were used in the local refinement for S2P spike complexes with 4-18 and 5-24. The 4-8 interface was locally refined following particle subtraction without symmetry expansion, since it lacked C3 symmetry, using a mask over the same region. Particle subtraction did not improve the density in the local refinement of the 2-17 interface and was therefore not used in the final map refinement. The density at the interface was well-defined for S2P spike complexes with 1-87, 4-8, 4-18 and 5-24, providing structural details of antibody binding to NTD. The 2-17 interface density allowed for fitting of the main chain but did not provide enough detail to confidently fit side chains, which were left out of the model in that region.

SARS CoV-2 S2P spike density was modeled using PDB entry 6VXX (Walls et al., 2020), as initial template. The RBDs and were initially modeled using PDB entry 7BZ5 (Wu et al., 2020); the NTDs were initially modeled using PDB entry 6ZGE (Wrobel et al., 2020). The initial models for all Fab variable regions were obtained using the SAbPred server (Dunbar et al., 2016).

Automated and manual model building were iteratively performed using real space refinement in Phenix (Adams et al., 2004) and Coot (Emsley and Cowtan, 2004) respectively. Geometry validation and structure quality assessment were performed using EM-Ringer (Barad et al., 2015) and Molprobity (Davis et al., 2004). Map-fitting cross correlation (Fit-in-Map tool) and figures preparation were carried out using PyMOL and UCSF Chimera (Pettersen et al., 2004) and Chimera X (Pettersen et al., 2021). A summary of the cryo-EM data collection, reconstruction and refinement statistics is shown in Table S1.

X-ray crystallography sample preparation, data collection, structure solution and refinement

Purified SARS-CoV-2 spike N-terminal domain (NTD) and 2-51 Fab were mixed at a 1:1 molar ratio and incubated at 4°C for 1 h; the Fab-NTD complex was purified by SEC on a Superdex 200 column in buffer 10 mM Tris, 150 mM NaCl, pH 7.4. Fractions containing the complex were combined and concentrated to a total protein concentration of 7.5 mg/mL for crystal screening by the sitting drop vapor diffusion method at 25°C. Diffracting crystals of NTD in complex with 2-51 Fab grew in 0.16 M calcium acetate, 0.08 M sodium cacodylate, 14.4% PEG 8000, 20% glycerol, pH 6.5. For data collection, crystals were cryo-protected by briefly soaking in reservoir solution supplemented with 35% (v/v) glycerol before flash-cooling in liquid nitrogen. X-ray diffraction data was collected to 3.44 Å resolution at 100 K from a single flash-cooled crystal on beamline 24ID-C at the Advanced Photon Source (APS) at Argonne National Laboratory. Diffraction data were processed with XDS (Kabsch, 2010) and scaled using AIMLESS (Evans and Murshudov, 2013) from the CCP4 software suite (Winn et al., 2011). Molecular replacement was performed with Phaser (McCoy, 2007) using the structure of NTD in complex with 4A8 (extracted from the whole spike-Fab structure from PDB entry 7C2L) as search model. Structure refinement was performed with a 3.65 Å high-resolution cutoff using Phenix refine (Adams et al., 2010) and PDB-redo (Joosten et al., 2014) alternated with manual model building using Coot. The Molprobity server was used for geometry validation and structure quality assessment. A summary of the X-ray crystallography data collection and refinement statistics is shown in Table S2.

Calculation of antibody angle of approach

The angles of antibody approach to the NTD of SARS-CoV-2 spike were calculated with UCSF Chimera (Pettersen et al., 2004). To define the latitudinal and longitudinal access of an antibody to the viral spike, we first defined two reference axes: the 3-fold axis of the spike trimer and a line perpendicular to the 3-fold axis and passing through the $C\alpha$ atom of Trp104 located in the hydrophobic core of the NTD. We then defined the axis of antibody as the long axis of the Fab. The latitudinal access, which describes the freedom between the viral and host cell membranes, was defined as the angle between the antibody axis and the 3-fold axis; the longitudinal access, which describes the freedom within the plane of the membrane, was defined as the angle between the antibody axis and the other reference axis. The angles between two axes were calculated with the built-in function of UCSF Chimera, and expressed in 0-to-180-degree scale for the latitudinal angles and 0-to-360-degree scale counter-clockwise to show the longitudinal angles. To compare the relative orientations of antibody heavy and light chains, we used a vector going from the center of heavy chain variable domain to that of the light chain variable domain.

Glycan analysis

To estimate the effect of glycan shield on protein surface residue, we used an in-house algorithm, GLYCO, to quantify the number of glycan atoms associated with each residue. Briefly, the number of glycan atoms per protein surface residue was counted within 34 Å radius distance cutoff, while the glycans do not provide the shielding effect were excluded in the calculation. This analysis was performed on each trajectory of molecular dynamics simulation (Casalino et al., 2020) to average the glycan atom counts for each residue.

Interface definition and net charge computation

The residues of each antibody paratope and epitope were obtained by running PDBePISA (Krissinel and Henrick, 2007), with the default parameters. Cryo-EM structures were of sufficient resolution to define all epitopes, except for 1-68 and 2-17. The epitope of 1-68 was obtained by docking the structure of the homolog antibody 1-87 in complex with NTD in the locally refined EM map of 1-68:NTD and real-space refinement was used to orient the residues of 1-68 that differed from 1-87. The missing side chains

of 2-17 were added by CHARMM-GUI (Jo et al., 2008) and the structure was combined with NTD to produce a model for the complex; the NTD structure was obtained by template-based Swiss modeling (Waterhouse et al., 2018). The hydrophobic interaction residues among antibodies were defined by the buried surface area (BSA) that large than 20 Å^2. The antigen contact region for germline genes were adopt from (Sela-Culang et al., 2013), which includes additional interactions not accounted for in the CDRs. The number of charged residues were counted and the summation of their charges was used to quantify the net charge of selected residues.

Cα distance calculation
The Cα distances per residue between superimposed ligand-free and antibody-bound NTD were calculated by Python 3.8. The 8 NTD-antibody complexes (NTD-5-24, NTD-4-8, NTD-2-17, NTD-4-18, NTD-1-87, NTD-4A8, NTD-2-51, NTD-1-68) were used as antibody bound structures, and the averaged Cα distances per residue of 8 complexes were analyzed.

RMSD calculation
The root mean square deviation (RMSD) of antibody epitopes was calculated by PyMOL 2.4 between two superimposed NTDs – ligand-free and antibody-bound structures. The identical ligand-free and antibody-bound NTDs described in Cα distance analysis were used in the calculation. Only matching atoms with the same name and number in both epitopes were included in the calculation. The epitope residues of antibodies were obtained by running FreeSASA (Mitternacht, 2016) with probe radius 1.4 Å. The residues with non-zero surface area difference between NTD and NTD-antibody complex structures were selected as protein epitope residues to the corresponding antibodies.

Sequence entropy of betacoronavirus spike
Human coronavirus reference amino acid sequences of OC43 (UniProt ID: P36334), HKU1 (UniProt ID: Q5MQD0), SARS (UniProt ID: P59594), and MERS (UniProt ID: W5ZZF5), as well as the initial SARS-CoV-2 (GenBank: QHO60594.1) sequence reported in Washington state were aligned using MAFFT software with default parameters (Katoh et al., 2002). Subsequently, we used the R bio3d package's function Conserv with default parameters to estimate sequence conservation at all alignment position

QUANTIFICATION AND STATISTICAL ANALYSIS

The statistical analyses for the pseudovirus and authentic virus neutralization assessments were performed using GraphPad Prism for calculation of mean value and SEM for each data point (see Figures S1 and S6). The SPR data were fitted using Biacore Evaluation Software (see Figure S6), and Scrubber (see Table S6). Cryo-EM data were processed and analyzed using cryoSPARC and Relion (see Figure S3). Cryo-EM and crystallographic structural statistics were analyzed using Phenix, Molprobity, EMringer and Chimera (see Tables S1 and S2). Statistical details of experiments are described in Method Details or Figure Legends.